




Simulating scalar field theories on quantum computers with limited resources

Andy C. Y. Li , Alexandru Macridin , Stephen Mrenna , and Panagiotis Spentzouris
Fermi National Accelerator Laboratory, Batavia, Illinois 60510, USA



(Received 20 October 2022; accepted 26 January 2023; published 3 March 2023)

We present a quantum algorithm for implementing ϕ^4 lattice scalar field theory on qubit computers. The field is represented in the discretized field amplitude basis. The number of qubits and elementary gates required by the implementation of the evolution operator is proportional to the lattice size. The algorithm allows efficient ϕ^4 state preparation for a large range of input parameters in both the normal and broken-symmetry phases. The states are prepared using a combination of variational and adiabatic evolution methods. First, the ground state of a local Hamiltonian, which includes the ϕ^4 self-interaction, is prepared using short variational circuits. Next, this state is evolved by switching on the coupling between the lattice sites adiabatically. The parameters defining the local Hamiltonian are adjustable and constitute the input of our algorithm. We present a method to optimize these parameters in order to reduce the adiabatic time required for state preparation. For preparing broken-symmetry states, the adiabatic evolution problems caused by crossing the phase transition critical line and by the degeneracy of the broken-symmetry ground state can be addressed using an auxiliary external field which gradually turns off during the adiabatic process. We show that the time dependence of the external field during the adiabatic evolution is important for addressing the broken-symmetry ground state degeneracy. The adiabatic time dependence on the inverse error tolerance can be reduced from quadratic to linear by using a field strength that decreases exponentially in time relative to one that decreases linearly.

DOI: [10.1103/PhysRevA.107.032603](https://doi.org/10.1103/PhysRevA.107.032603)

I. INTRODUCTION

Simulating highly entangled quantum systems is among the first applications of quantum computers expected to show a practical advantage over classical computers [1,2]. The development and application of new quantum processors [3–5] may allow for revolutionary calculations in quantum chemistry [6–11], condensed-matter physics [12–17], nuclear physics [18,19] and high-energy physics [20–24]. The simulation of relativistic quantum field theory on quantum hardware [20,21,24–27] has been an active research topic in recent years. In practice, the mapping and preparation of continuous fields on near-future quantum hardware of limited size and with limited control fidelity provides a number of challenges. In this paper, we address the simulation of the ϕ^4 scalar field on digital quantum computers.

The ϕ^4 scalar field model [28,29] is a simplified model of the Higgs field of the standard model of particle physics and has been intensively studied over the years. Despite its apparent simplicity, it has rich physics. For example, in $(1+1)$ and $(2+1)$ space-time dimensions, it exhibits a phase transition to a broken symmetry phase characterized by a finite vacuum expectation value $\langle\phi\rangle$ [30,31]. Perturbative methods based on a diagrammatic expansion are only valid in the weak interaction regime. As a result, the strong interacting regime has been studied numerically. Calculations of the critical coupling and exponent for $(1+1)$ dimensions have been performed using DMRG [32], tensor network methods [33,34], Monte Carlo methods [35,36] and diagonalization methods [37,38]. However, since the Hilbert space of the ϕ^4 model is exponentially large, the field degrees of freedom must be truncated, making

the extrapolation of the numerical results to the continuous limit challenging and not always reliable.

Quantum simulations can overcome the size problems related to the Hilbert space and, unlike most classical Monte Carlo methods, can calculate the real-time correlations and nonequilibrium dynamics of the system. The bosonic fields can be represented efficiently on qubits in a discretized field amplitude basis [12,13,39]. However the preparation of field eigenstates on qubits is not straightforward. For example, the method proposed in Refs [20,26,27] prepares an initial noninteracting multivariate Gaussian state and uses adiabatic continuation to reach the desired interacting state. However, the construction of a multivariate Gaussian wave function using the Kitaev-Webb method [40] requires a very large number of qubits and is not feasible on near-term quantum hardware. Moreover, the preparation of broken-symmetry states using adiabatic continuation of noninteracting states is challenging since the adiabatic path has to cross a critical region with a vanishing excitation gap. Furthermore, the ground state of broken-symmetry states is degenerate, causing further complications.

Here, we present a quantum algorithm for lattice ϕ^4 field evolution on qubits and a method for initial state preparation suitable for near-term quantum computers. A relatively small number of qubits per lattice site, $n_q \approx 6 \sim 8$, is sufficient to address even strong-coupling regimes. The number of qubits and the number of gates scale proportionally to the system size N . The most expensive part of the algorithm arises from the implementation of the ϕ^4 interaction, which requires $O(N n_q^4)$ two-qubit gates, while the implementation of the other terms in the Hamiltonian requires $O(N n_q^2)$ two-qubit gates. The field

state preparation combines variational and adiabatic evolution approaches. The Hamiltonian is split into two parts, a local one that sums contributions from each individual site and a nonlocal one containing coupling between sites. The adiabatic process starts from the ground state of the local Hamiltonian. Then the coupling between sites is turned on adiabatically. Unlike previous approaches in the literature [20], our method introduces self-interactions from the start. The ground state of the local Hamiltonian is prepared accurately using short variational circuits. Instead of preparing the full lattice states using variational ansatzes [41], which would be difficult to scale up due to Barren plateaus [42], our variational circuits prepare local states. The calculation of these circuits' parameters is independent of the system size and can be done easily on classical computers using various optimization methods. The input parameters of the local Hamiltonian can be adjusted to minimize the time of the adiabatic process. We find a direct correlation between the adiabatic time and the local overlap of the initial wave function and the target wave function. We propose a strategy to determine the optimal parameters of the local Hamiltonian by maximizing this local overlap.

We also address the problems associated with the preparation of the broken-symmetry states, namely, the crossing of the critical phase transition region characterized by a vanishing excitation gap and the double degeneracy of the broken-symmetry state. Both of these problems can be mitigated by coupling the scalar field to an external field. We propose a two step adiabatic process for preparing broken-symmetry states. The first adiabatic process starts from a local state in the presence of a significant external field. Then, adiabatically, the intersite coupling term is turned on and the external field is decreased. Due to the presence of the external field, the excitation gap is robust during this process. The second adiabatic process starts from the terminus of the first one. During this step the external field is decreased to vanishing values. We find a reduction of the required adiabatic time from $O(\varepsilon^{-2})$ to $O(\varepsilon^{-1} \ln[\varepsilon^{-1}])$ with ε being the error bound when the external field decreases exponentially in time compared to the case of linear decrease in time.

This paper is organized as follows. We review the ϕ^4 model and its lattice discretization in Sec. II. We then discuss the qubit encoding and circuits to simulate the scalar field evolution on quantum computers in Sec. III. In Sec. IV we introduce our state preparation protocol consisting of the variational local-state preparation (Sec. IV A) and adiabatic evolution for the normal phase (Sec. IV B 1) and for the broken-symmetry phase (Sec. IV B 2) supported by numerical simulation of the lattice ϕ^4 model with up to four sites. Our summary and conclusions are provided in Sec. V.

II. THE ϕ^4 MODEL

The Hamiltonian density of the ϕ^4 model can be written as ($\hbar = c = 1$)

$$\mathbb{H} = \frac{1}{2}\pi^2 + \frac{1}{2}m_b^2\phi^2 + \frac{1}{2}(\nabla\phi)^2 + \frac{\lambda_b}{4!}\phi^4 + f_b\phi, \quad (1)$$

where m_b and λ_b are the unrenormalized (bare) mass and interaction strength, respectively. In order to investigate the broken-symmetry phase, it is convenient to consider a cou-

pling term between the scalar field and an external field f_b . The field operator ϕ and the conjugate-field operator π obey the commutation relation,

$$[\pi(x), \phi(y)] = i\delta(x - y). \quad (2)$$

For quantum simulation, we consider the lattice version of the ϕ^4 model in $d + 1$ spacetime dimensions given by

$$H_{\text{lat}} = a^d \sum_j \left[\frac{1}{2}\pi_j^2 + \frac{1}{2}m_b^2\phi_j^2 + \frac{1}{2a^2} \sum_{e=1}^d (\phi_{j+e} - \phi_j)^2 + \frac{\lambda_b}{4!}\phi_j^4 + f_b\phi_j \right], \quad (3)$$

where a is the lattice constant and j labels lattice sites. The label $j + e$ represents the next-nearest neighbor site of the site j in the direction e . Note that in Eq. (3) only the space dimension is discretized and on a lattice. This differs from most models employed in Monte Carlo-based simulations, where both space and imaginary time dimensions are discretized on a lattice. Nonetheless, the implementation of our algorithm on quantum computers also requires time discretization, consequence of the Trotter-Suzuki expansion [43–45] of the time evolution operator. The lattice field operators in Eq. (3) obey the commutation relations

$$[\phi_i, \pi_j] = ia^{-d}\delta_{i,j} \quad \text{and} \quad [\phi_i, \phi_j] = [\pi_i, \pi_j] = 0. \quad (4)$$

The continuous limit is achieved by taking $a \rightarrow 0$. It is convenient to introduce dimensionless field variables

$$\bar{\Phi}_j = a^{\frac{d-1}{2}}\phi_j \quad \text{and} \quad \bar{\Pi}_j = a^{\frac{d+1}{2}}\pi_j \quad (5)$$

which obey the canonical commutation relations

$$[\bar{\Phi}_i, \bar{\Pi}_j] = i\delta_{i,j} \quad \text{and} \quad [\bar{\Phi}_i, \bar{\Phi}_j] = [\bar{\Pi}_i, \bar{\Pi}_j] = 0. \quad (6)$$

Using these dimensionless operators, the Hamiltonian is given by

$$\bar{H} = \sum_j \left[\frac{1}{2}\bar{\Pi}_j^2 + \frac{1}{2}m_0^2\bar{\Phi}_j^2 + \frac{1}{2} \sum_{e=1}^d (\bar{\Phi}_{j+e} - \bar{\Phi}_j)^2 + \frac{\lambda_0}{4!}\bar{\Phi}_j^4 + f_0\bar{\Phi}_j \right], \quad (7)$$

where $\bar{H} \equiv H_{\text{lat}}a$, $m_0^2 \equiv m_b^2a^2$, $\lambda_0 \equiv \lambda_b a^{3-d}$, and $f_0 \equiv f_b a^{(3+d)/2}$ are dimensionless. This Hamiltonian (with $f_0 = 0$) was previously used in numerical simulations of the scalar field model [25,33]. It represents a set of coupled harmonic oscillators with an anharmonic interaction.

The correlation length is a measurable parameter which determines how the correlation between the field values at two separate points decays with the distance between these points. To extrapolate the lattice results to a meaningful continuous limit with a finite correlation length, it is necessary to simulate large lattices for Hamiltonian parameters corresponding to large lattice correlation lengths (measured in units of a). The physics of the ϕ^4 theory is extracted from the lattice results by taking $a/\xi \rightarrow 0$ (continuous limit) and $L/\xi \rightarrow \infty$ (macroscopic limit), where L is the lattice size and ξ is the lattice correlation length. Equivalently, this implies simulations with

$m_p a \rightarrow 0$ and $m_p a \gg 1/N$ where N is the number of lattice sites per dimension and $m_p \propto 1/\xi$ is the physical mass.

While the lattice physical parameters are needed for the extrapolation from the lattice to the continuous theory, the bare parameters define the input of the simulations. To be useful, a quantum algorithm should be able to prepare efficiently quantum states for a large range of bare parameters, including both negative and positive input parameter m_0^2 . In principle, the relation between the physical and the bare parameters can be established from simulations, since the lattice physical parameters can be extracted from the correlation functions. For the extrapolation to the continuous limit the bare lattice parameters need to be chosen dependent on the lattice constant a . This dependence is significant since the renormalization theory shows that, in order to extrapolate to a continuous theory with finite physical observables, the bare parameters diverge with $a \rightarrow 0$ in many cases. For example, in (1 + 1) and (2 + 1) dimensions, the bare squared mass m_0^2 becomes negative and proportional to $\ln(m_p a)$ and $-1/(m_p a)$, respectively [46], for small a .

The ϕ^4 model (with $f_0 = 0$) has a discrete Z_2 symmetry from the transformation $\phi \rightarrow -\phi$. In (3 + 1) dimensions, the theory is “believed” to be trivial (i.e., the theory is actually noninteracting in the continuum limit), although no rigorous proof exists [47–51]. For higher dimensions, the triviality can be rigorously proven [28]. In (1 + 1) and (2 + 1) dimensions, the model exhibits a phase transition from a symmetric state with $\langle \phi \rangle = 0$ to a broken-symmetry phase with finite $\langle \phi \rangle$ [30,31]. However, in finite size systems, like the ones used for simulations, the ground state cannot have a broken symmetry and there is no phase transition. Nonetheless, the broken-symmetry phase can be investigated numerically by considering the coupling term $f_0 \Phi$ in Eq. (7) and extrapolating the results to the large lattice size ($L \rightarrow \infty$) and the zero external field ($f_0 \rightarrow 0$) limits.

It is interesting that, for negative values of m_0^2 and small interaction strength (i.e., when $|m_0|^3/\lambda_0 \gg 1$), the ground state is nearly twofold degenerate and exhibits properties characteristic of the broken-symmetry phase even for small lattices. A single site system reduces to a double-well potential Hamiltonian for negative m_0^2 . The field distribution in the ground state is symmetric and double-peaked around zero, with the two maxima located at the points $\pm \bar{\Phi}_m$ which minimize the potential. The gap is small, decreasing exponentially fast with increasing magnitude of $|m_0|^3/\lambda_0$. A small external field f_0 (of the order of the gap) coupled to the scalar field amplitude produces a ground state with finite $\langle \Phi \rangle \approx \bar{\Phi}_m$ (or $\langle \Phi \rangle \approx -\bar{\Phi}_m$, depending on f_0 sign). Numerical calculations of small size systems show that the system remains nearly twofold degenerate when the number of sites is increased. The gap decreases with an increasing number of sites, while the energy difference between the second and the first excited states does not decrease, as can be seen in Fig. 1. This is a consequence of the kinetic term in the Hamiltonian [the third term in Eq. (7)] which favors similar field configurations at neighboring sites. These properties of small size systems allows us to investigate quantum state preparation methods for broken-symmetry phase by using classical simulations of small lattices, as discussed in Sec. IV B 2.

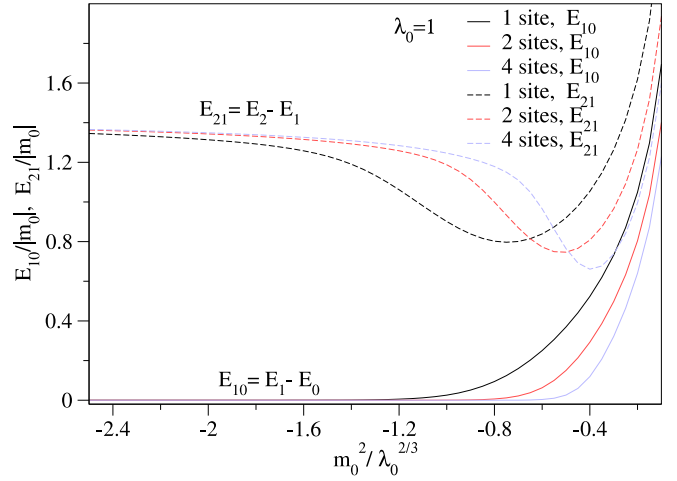


FIG. 1. The gap, $E_{10} = E_1 - E_0$, and the energy difference between the second and the first excited states, $E_{21} = E_2 - E_1$, for one-site, two-site, and four-site ϕ^4 lattices for negative values of m_0^2 . The system is nearly double degenerate when $m_0^2/\lambda_0^{2/3} \ll -1$. The gap decreases exponentially with increasing the magnitude of $|m_0^2|$. On the other hand, E_{21} increases slightly with increasing the magnitude of $|m_0^2|$. With increasing the number of sites, the gap E_{10} decreases while E_{21} increases.

III. Φ^4 FIELD ON QUBITS

This section describes the qubit encoding of the bosonic states and the implementation of the evolution operator corresponding to the lattice Hamiltonian H_{lat} in Eq. (7). Discretizing continuous groups is important for simulating quantum field theories and has been studied for several models [52–54]. The representation of bosonic fields on qubits was discussed in detail in [39]. We will review briefly the general methodology in Sec. III A, present the qubit encoding in Sec. III B, and address the evolution operator implementation in Sec. III C.

A. Finite representation of bosonic fields

The lattice Hilbert space is a direct product of local Hilbert spaces (one at each lattice site) such that $\mathcal{H} = \prod_{j=1}^N \otimes \mathcal{H}_j$, where j labels the lattice site and N is the number of lattice sites. A local Hilbert space \mathcal{H}_j is infinite dimensional. The number of bosons contributing to the wave function is, in principle, unbounded. However, since we are interested in the low-energy physics of the system, we postulate that, at every lattice site, the number of bosons can be truncated with negligible error by a cutoff number N_b .

The eigenvectors $\{|\varphi\rangle_j\}$ of the field operator,

$$\bar{\Phi}_j |\varphi\rangle_j = \varphi |\varphi\rangle_j, \quad (8)$$

form a convenient basis choice for representing the evolution operator since the Hamiltonian interaction terms are diagonal in this basis. However, the eigenvalues $\varphi \in \mathbb{R}$ are continuous and unbounded. Therefore, discretization procedures are necessary to represent the truncated Hilbert space in the field amplitude basis. We introduce the discretization procedure below.

The low-energy subspace of the local Hilbert space \mathcal{H}_j is spanned by the states with a number of bosons below the cutoff N_b and can be represented with good accuracy by a finite Hilbert space \mathcal{H}_j of dimension N_φ , with $N_\varphi > N_b$, as described below. Let $\{|\varphi_\alpha\rangle_j\}$ be a set of orthonormal vectors belonging to \mathcal{H}_j with $\alpha \in \{0, 1, \dots, N_\varphi - 1\}$. We define the *discrete field operators* Φ_j and Π_j acting on \mathcal{H}_j as

$$\Phi_j|\varphi_\alpha\rangle_j = \varphi_\alpha|\varphi_\alpha\rangle_j, \quad (9)$$

$$\Pi_j = \mu\mathcal{F}_j\Phi_j\mathcal{F}_j^{-1}, \quad (10)$$

where φ_α is the discrete eigenvalue,

$$\varphi_\alpha = \Delta_\varphi \left(\alpha - \frac{N_\varphi - 1}{2} \right), \quad \alpha \in \{0, 1, \dots, N_\varphi - 1\}, \quad (11)$$

$$\Delta_\varphi = \sqrt{\frac{2\pi}{N_\varphi\mu}}, \quad (12)$$

and \mathcal{F}_j is the finite Fourier transform,

$$\mathcal{F}_j = \frac{1}{\sqrt{N_\varphi}} \sum_{\alpha, \beta=0}^{N_\varphi-1} e^{i\frac{2\pi}{N_\varphi}(\alpha - \frac{N_\varphi-1}{2})(\beta - \frac{N_\varphi-1}{2})} |\varphi_\alpha\rangle_j \langle\varphi_\beta|_j. \quad (13)$$

In Eq. (10), $\mu > 0$ is the boson mass which is the parameter entering in the definition of the lattice boson creation and annihilation operators,

$$a_j^\dagger = \sqrt{\frac{\mu}{2}}\bar{\Phi}_j - i\sqrt{\frac{1}{2\mu}}\bar{\Pi}_j, \quad a_j = \sqrt{\frac{\mu}{2}}\Phi_j + i\sqrt{\frac{1}{2\mu}}\Pi_j. \quad (14)$$

The definition of Φ_j given by Eqs. (9), (11), and (12) represents the discretized and truncated version of Eq. (8). The set of states $\{|\kappa_\beta\rangle_j\}_{\beta \in \{0, 1, \dots, N_\varphi-1\}}$ obtained by applying the Fourier transform to the set $\{|\varphi_\alpha\rangle_j\}$,

$$\begin{aligned} |\kappa_\beta\rangle_j &\equiv \mathcal{F}_j|\varphi_\beta\rangle_j \\ &= \frac{1}{\sqrt{N_\varphi}} \sum_{\alpha=0}^{N_\varphi-1} e^{i\frac{2\pi}{N_\varphi}(\alpha - \frac{N_\varphi-1}{2})(\beta - \frac{N_\varphi-1}{2})} |\varphi_\alpha\rangle_j, \end{aligned} \quad (15)$$

are the eigenvectors of the discrete conjugate-field operator Π_j defined by Eq. (10) such that

$$\Pi_j|\kappa_\beta\rangle_j = \kappa_\beta|\kappa_\beta\rangle_j, \quad (16)$$

where

$$\kappa_\beta = \Delta_\kappa \left(\beta - \frac{N_\varphi - 1}{2} \right), \quad \beta \in \{0, 1, \dots, N_\varphi - 1\}, \quad (17)$$

$$\Delta_\kappa = \sqrt{\frac{2\pi\mu}{N_\varphi}}. \quad (18)$$

Equation 16 is the discretized version of the conjugate-field operator eigenvalue equation, $\bar{\Pi}_j|\kappa\rangle_j = \kappa|\kappa\rangle_j$, with continuous and unbounded $\kappa \in \mathbb{R}$.

Different representations corresponding to different values of μ can be chosen to construct the finite representation. For a given problem and desired accuracy, the cutoff N_b depends on the boson mass μ . In principle μ should be optimized for the lowest possible cutoff N_b to reduce the computing resources. Moreover, as can be seen from Eqs. (12) and (18), the discretization interval Δ_φ of the field amplitude variable and the

discretization interval Δ_κ of the conjugate-field variable are also dependent on the boson mass parameter μ . The parameter μ can be tuned to adjust the accuracy of the discretization. Increasing μ decreases the field variable discretization interval and increases the conjugate-field discretization interval. The discretized field and conjugate-field variables are related by a finite Fourier transform, thus $\Delta_\varphi\Delta_\kappa = 2\pi/N_\varphi$. To decrease both discretization intervals, Δ_φ and Δ_κ , the number of discretization points N_φ should be increased. For quantum simulations, tuning μ to increase the accuracy of the wave function's discretization is much easier than the process of optimizing μ to decrease the boson number cutoff N_b , as discussed in [39].

On the subspace of \mathcal{H}_j spanned by the first N_b eigenstates of the harmonic oscillator Hamiltonian ($H_{hj} = \frac{1}{2}\Pi_j^2 + \frac{1}{2}\mu^2\Phi_j^2$), the discrete field and conjugate-field operators obey, with $O(\epsilon)$ accuracy, the canonical commutation relation,

$$I_{N_b}[\Phi_j, \Pi_j]I_{N_b} = iI_{N_b} + O(\epsilon). \quad (19)$$

Here I_{N_b} is the projector on the N_b size low-energy subspace of the harmonic oscillator. This is a consequence of the Nyquist-Shannon sampling theorem applied to the fast decaying boson number wave functions, as discussed in [39]. For a problem of interest, as long as N_b is taken large enough such that the contribution of states with more than N_b bosons can be neglected, the infinite Hilbert space \mathcal{H}_j can be replaced by the finite N_φ -size Hilbert space \mathcal{H}_j , and the lattice field operators $\bar{\Phi}_j$ and $\bar{\Pi}_j$ [Eq. (5)] can be replaced by the discrete operators Φ_j and Π_j [Eqs. (9) and (10)] with $O(\epsilon)$ accuracy. For a fixed N_b , the error $O(\epsilon)$ decreases exponentially by increasing N_φ . For practical purpose, we find numerically that a number of discretization points $N_\varphi = 2N_b$ yields an accuracy of order 10^{-4} .

The finite lattice representation is given by the finite Hilbert space $\mathcal{H} = \prod_{j=1}^N \otimes \mathcal{H}_j$ of dimension N_φ^N and the set of local field and conjugate field-operators $\{\Phi_j\}_{j \in \{1, 2, \dots, N\}}$ and $\{\Pi_j\}_{j \in \{1, 2, \dots, N\}}$ defined by Eq. (9) and Eq. (10), respectively. The discretized field amplitude basis vectors are

$$|\varphi_\alpha\rangle \equiv |\varphi_{\alpha_1}\rangle_1 |\varphi_{\alpha_2}\rangle_2 \cdots |\varphi_{\alpha_N}\rangle_N, \quad (20)$$

where

$$\alpha = \{\alpha_1, \alpha_2, \dots, \alpha_N\} \text{ with } \alpha_j \in \{0, 1, \dots, N_\varphi - 1\}. \quad (21)$$

B. Qubit encoding of the finite representation

The discretized field amplitude basis $\{|\varphi_\alpha\rangle\}$ [Eq. (20)] can be encoded on qubits using the binary representation of the label α [Eq. (21)]. For each site, a register of $n_q = \log_2(N_\varphi)$ qubits is assigned. A local field amplitude state $|\varphi_{\alpha_j}\rangle_j$ at site j is encoded as

$$|\varphi_{\alpha_j}\rangle_j \equiv |\alpha_{0j}\rangle_j |\alpha_{1j}\rangle_j \cdots |\alpha_{(n_q-1)j}\rangle_j, \quad (22)$$

where $|\alpha_{qj}\rangle_j \in \{|0\rangle, |1\rangle\}$ is the q th qubit state from the register j (i.e., allocated to represent the field at the site j) such that

$$\alpha_j = \sum_{q=0}^{n_q-1} \alpha_{qj} 2^{n_q-1-q}. \quad (23)$$

Note that the binary variables $\alpha_{qj} \in \{0, 1\}$ defined by Eq. (23) yield the binary representation of the integer $\alpha_j \equiv [\alpha_{0j}\alpha_{1j}\cdots\alpha_{(n_q-1)j}]$. A lattice state [Eq. (20)] is encoded as a direct product of N local states encoded by Eq. (22). The lattice states require $N \log_2(N_\varphi)$ qubits for encoding.

The discrete field operator Φ_j acting on the n_q qubits assigned to encode the field at site j can be written as

$$\Phi_j = -\Delta_\varphi \sum_{q=0}^{n_q-1} 2^{n_q-1-q} \frac{\sigma_{qj}^z}{2}, \quad (24)$$

where $\sigma_{qj}^z = |0\rangle\langle 0|_{qj} - |1\rangle\langle 1|_{qj}$ is the Pauli Z operator and q is the qubit index. It can be directly checked that Φ_j defined here and the vector encoded as in Eq. (22) satisfy the eigenvalue equation defined by Eqs. (9) and (11).

The definition of the conjugate-field operator Π_j on the qubit space requires first the qubit implementation of the Fourier transform \mathcal{F}_j [see Eq. (10)]. The implementation of Quantum Fourier transform (QFT) on qubits is well known [55]. However, the Fourier transform \mathcal{F}_j defined by Eq. (13) is centered, i.e., the summation index runs from $-(N_\varphi - 1)/2$ to $(N_\varphi - 1)/2$, unlike the off-centered QFT where the summation index runs from 0 to $N_\varphi - 1$. As shown in Appendix A, the Fourier transform is related to the QFT by

$$\begin{aligned} \mathcal{F}_j &= e^{-i\frac{N_\varphi\delta^2}{2\pi}} \prod_{q=0}^{n_q-1} R_{qj}^z(2^{n_q-1-q}\delta) \text{QFT}_j \\ &\times \prod_{q=0}^{n_q-1} R_{qj}^z(2^{n_q-1-q}\delta), \end{aligned} \quad (25)$$

where $\delta = \pi \frac{N_\varphi-1}{N_\varphi}$ and R_{qj}^z is a single-qubit z rotation acting on the qubit q at site j given by

$$R_{qj}^z(\theta) \equiv e^{-i\theta \frac{\sigma_{qj}^z}{2}} = e^{-i\frac{\theta}{2}} |0\rangle\langle 0|_{qj} + e^{i\frac{\theta}{2}} |1\rangle\langle 1|_{qj}. \quad (26)$$

According to Eq. (10), the discrete conjugate-field operator is

$$\Pi_j = \mathcal{F}_j \left(-\Delta_k \sum_{q=0}^{n_q-1} 2^q \frac{\sigma_{qj}^z}{2} \right) \mathcal{F}_j^{-1}. \quad (27)$$

Note that the factor before Pauli σ_{qj}^z gate is 2^q , unlike the factor in Eq. (24) which is 2^{n_q-1-q} . This is caused by the fact that the qubit order is reversed after a QFT gate (unless additional swap operations are performed to manually reverse the qubit order) [55].

C. Evolution operator

In order to implement the evolution operator we employ the Trotter-Suzuki expansion [43–45]. The evolution operator is written as a product of short-time evolution operators corresponding to the different terms in the Hamiltonian, called Trotter steps. Here we present the qubit implementation of the Trotter steps corresponding to the different terms present in the ϕ^4 Hamiltonian.

We start with the operator $e^{-i\theta\Phi_j}$, where θ is the time interval of the Trotter step. This Trotter step implements the

evolution of the term $f_0\Phi_j$ in Eq. (7). Employing Eq. (24) one has

$$e^{-i\theta\Phi_j} = \prod_{q=0}^{n_q-1} R_{qj}^z(-2^{n_q-1-q}\Delta_\varphi\theta). \quad (28)$$

It reduces to n_q single-qubit z rotations.

The Trotter step $e^{-i\theta\Phi_j^2}$ can be written as

$$e^{-i\theta\Phi_j^2} = e^{-i\theta\Delta_\varphi^2 \frac{N_\varphi^2-1}{12}} \prod_{p=0}^{n_q-1} \prod_{q=0}^{p-1} \mathbb{Z}_{pj;qj}(v_{pq}), \quad (29)$$

where

$$\mathbb{Z}_{pj;qj}(v) = e^{-iv\sigma_{pj}^z\sigma_{qj}^z} \quad (30)$$

$$v_{pq} = 2^{2n_q-3-p-q}\Delta_\varphi^2\theta. \quad (31)$$

The two-qubit gate $\mathbb{Z}_{pj;qj}$ acts on the qubit p at site j and on the qubit q at site j . Note that one $\mathbb{Z}_{pj;qj}$ can be decomposed into two CNOT gates and one R^z gate [56]. Hence, the Trotter step Eq. (29) consists of $n_q(n_q - 1)$ CNOT gates.

The implementation of the Trotter step $e^{-i\theta\Pi_j^2}$ is given by

$$\begin{aligned} e^{-i\theta\Pi_j^2} &= \mathcal{F}_j e^{-i\mu\theta\Phi_j^2} \mathcal{F}_j^{-1} \\ &= e^{-i\theta\Delta_\kappa^2 \frac{N_\varphi^2-1}{12}} \mathcal{F}_j \left[\prod_{p=0}^{n_q-1} \prod_{q=0}^{p-1} \mathbb{Z}_{pj;qj}(v'_{pq}) \right] \mathcal{F}_j^{-1}, \end{aligned} \quad (32)$$

where $v'_{pq} = 2^{p+q-1}\theta\Delta_\kappa^2$. The \mathbb{Z} gate's parameter v'_{pq} entering in Eq. (32) can be obtained from Eq. (30) by replacing $n_q - 1 - p \rightarrow p$ and $n_q - 1 - q \rightarrow q$, (consequence of reverse qubit order after applying QFT) and $\Delta_\varphi \rightarrow \Delta_\kappa$. Since QFT requires $n_q(n_q - 1)/2$ CNOT gates, this Trotter step consists of $3n_q(n_q - 1)$ CNOT gates.

The Trotter step $e^{-i\theta\Phi_j\Phi_l}$ corresponding to the coupling term between the sites j and l is

$$e^{-i\theta\Phi_j\Phi_l} = \prod_{p=0}^{n_q-1} \prod_{q=0}^{n_q-1} \mathbb{Z}_{pj;ql}(v''_{pq}), \quad (33)$$

where $v''_{pq} = 2^{2n_q-4-p-q}\theta\Delta_\varphi^2$. This Trotter steps consists of n_q^2 \mathbb{Z} gates or $2n_q^2$ CNOT gates. Since the interaction is not local, in this case the \mathbb{Z} gates act on one qubit belonging to the qubit register allocated for the field at site j and on one qubit belonging to the qubit register allocated for the field at site l .

The Trotter step corresponding to the ϕ^4 interaction term is

$$\begin{aligned} e^{-i\theta\Phi_j^4} &= \left[\prod_{p=0}^{n_q-1} \prod_{q=0}^{p-1} \prod_{r=0}^{q-1} \prod_{s=0}^{r-1} \mathbb{Z}\mathbb{Z}\mathbb{Z}\mathbb{Z}_{pj;qj;rj;s_j}(\rho_{qprs}) \right] \\ &\times \left[\prod_{p=0}^{n_q-1} \prod_{q=0}^{p-1} \mathbb{Z}_{pj;qj}(\eta_{pq}) \right] e^{i\xi}, \end{aligned} \quad (34)$$

where

$$\mathbb{Z}\mathbb{Z}\mathbb{Z}\mathbb{Z}_{pj;qj;rj;s_j}(\rho) = e^{-i\rho\sigma_{pj}^z\sigma_{qj}^z\sigma_{rj}^z\sigma_{sj}^z} \quad (35)$$

TABLE I. CNOT gates count of the Trotter steps required for the implementation of the ϕ^4 evolution operator. All-to-all qubit connectivity is assumed.

Operator	$e^{-i\Phi\theta}$	$e^{-i\Phi^2\theta}$	$e^{-i\Pi^2\theta}$	$e^{-i\Phi_j\Phi_k\theta}$	$e^{-i\Phi^4\theta}$
Number of CNOTS	0	$n_q^2 - n_q$	$3n_q^2 - 3n_q$	$2n_q^2$	$\frac{1}{4}n_q^4 - \frac{3}{2}n_q^3 + \frac{15}{4}n_q^2 - \frac{5}{2}n_q$

and

$$\rho_{pqrs} = \frac{3N_\varphi^4}{32} \frac{1}{2^{p+q+r+s}} \theta \Delta_\varphi^4, \quad (36)$$

$$\eta_{pq} = \frac{N_\varphi^4}{16} \frac{1}{2^{p+q}} \left(1 - \frac{1}{N_\varphi^2} - \frac{1}{2^{2p+1}} - \frac{1}{2^{2q+1}} \right) \theta \Delta_\varphi^4, \quad (37)$$

$$\xi = \left[\frac{(N_\varphi^2 - 1)^2}{48} - \frac{N_\varphi^4 - 1}{120} \right] \theta \Delta_\varphi^4. \quad (38)$$

This step requires $n_q(n_q - 1)(n_q - 3)(n_q - 3)/24$ four-qubit \mathbb{ZZZ} gates and $n_q(n_q - 1)/2$ two-qubit \mathbb{ZZ} gates.

Quantum simulation on near-term quantum devices is mainly limited by the two-qubit gate fidelities. The implementation of the Trotter step corresponding to the ϕ^4 interaction term is computationally the most expensive one, since it requires $O(n_q^4)$ of two-qubit gates. The number of CNOT gates for all Trotter steps relevant for the implementation of the ϕ^4 evolution are summarized in Table I. For comparison purpose, the \mathbb{ZZ} and the \mathbb{ZZZ} gates are decomposed in two-qubit CX (CNOT) gates and single-qubit R^z rotations [56],

$$\mathbb{ZZ}_{p,q}(v) = CX_{p,q} R_q^z(v) CX_{p,q}, \quad (39)$$

$$\begin{aligned} \mathbb{ZZZ}_{p,q,r;s}(\rho) &= CX_{p,q} CX_{q,r} CX_{r;s} R_s^z(\rho) \\ &\times CX_{r;s} CX_{q,r} CX_{p,q}. \end{aligned} \quad (40)$$

Since the number of Trotter steps is proportional to the lattice size, the computational cost of this algorithm scales linearly with N .

IV. STATE PREPARATION

This section addresses the preparation of the ground state on qubits for both normal and broken-symmetry phases. Our method combines variational quantum circuits and adiabatic evolution, and it is flexible enough to allow tuning of different parameters to minimize circuit depth. To prepare broken-symmetry states, an interaction between the scalar field and an external field is introduced that explicitly breaks the Z_2 symmetry. By properly choosing the strength of the external field as a function of time during the adiabatic process, the dual problems of degeneracy and broken symmetry in the ground state are mitigated, as we discuss in Sec. IV B 2.

The Hamiltonian H employed for the quantum simulations of the ϕ^4 model is given by (7) with the lattice field operators replaced by the discrete field operators, as described in Sec. III A. To prepare the ground state, we divide H in two

parts,

$$H = H_{\text{loc}} + H_c, \quad (41)$$

where

$$\begin{aligned} H_{\text{loc}} &= \sum_{j=1}^N H_{\text{loc},j} \\ &= \sum_{j=1}^N \left(\frac{1}{2} \Pi_j^2 + \frac{1}{2} m_j^2 \Phi_j^2 + \frac{\lambda_j}{4!} \Phi_j^4 + f_j \Phi_j \right), \quad (42) \\ H_c &= \sum_{j=1}^N \left[\frac{1}{2} \sum_{e=0}^d (\Phi_{j+e} - \Phi_j)^2 + \frac{1}{2} \delta m^2 \Phi_j^2 \right. \\ &\quad \left. + \frac{\delta \lambda}{4!} \Phi_j^4 + \delta f \Phi_j \right], \quad (43) \end{aligned}$$

where $\delta m^2 = m_0^2 - m_j^2$, $\delta \lambda = \lambda_0 - \lambda_j$, and $\delta f = f_0 - f_j$. The Hamiltonian H_{loc} is a sum of uncoupled local Hamiltonians $H_{\text{loc},j}$ acting only at the lattice site j . The input parameters, m_j^2 , λ_j and f_j should be chosen to ensure that the adiabatic evolution part of the state preparation is efficient, as we discuss in Sec. IV B. The first term in H_c couples the fields at neighboring sites, while the last three terms in H_c are local.

Our state preparation protocol consists of two parts.

(1) The ground state of H_{loc} is prepared using variational circuits, as we describe in Sec. IV A. It is a direct product of the ground state of $H_{\text{loc},j}$ at each lattice site j , $|\psi_g^{\text{loc}}\rangle_j$:

$$|\psi_g^{\text{loc}}\rangle = \prod_{j=1}^N \otimes |\psi_g^{\text{loc}}\rangle_j. \quad (44)$$

(2) The ground state of the full Hamiltonian is obtained by adiabatic evolution. The Hamiltonian H_c is turned on adiabatically. The system evolves under the time dependent Hamiltonian,

$$H(s) = H_{\text{loc}} + \alpha(s)H_c, \quad (45)$$

from $|\psi_g^{\text{loc}}\rangle$ to the ground state of the Hamiltonian Eq. (7). The time t enters in Eq. (45) via the variable $s = t/T$, where T is the total time of the adiabatic process and the function $\alpha(s)$ has boundary conditions $\alpha(0) = 0$ and $\alpha(1) = 1$ in the time interval T .

A. Variational preparation of local states

The ground state $|\psi_g^{\text{loc}}\rangle_j$ of the local Hamiltonian $H_{\text{loc},j}$ can be prepared accurately using short circuits on the n_q qubits assigned to represent the field at the site j . We propose a hardware-efficient circuit ansatz to prepare the local ground state using one- and two-qubit gates. The circuit parameters are determined using optimization algorithms on classical computers, as discussed below.

First, the local wave function in the discrete field amplitude basis, $\langle \varphi_\alpha | \psi_g^{\text{loc}} \rangle_j$ with $\alpha \in \{0, 1, \dots, N_\varphi - 1\}$, is calculated on a classical computer. This requires the diagonalization of a small size $N_\varphi \times N_\varphi$ matrix corresponding to the Hamiltonian $H_{\text{loc},j}$.

Second, parameterized quantum circuits are employed to produce n_q -qubit quantum states. We consider circuit ansatzes

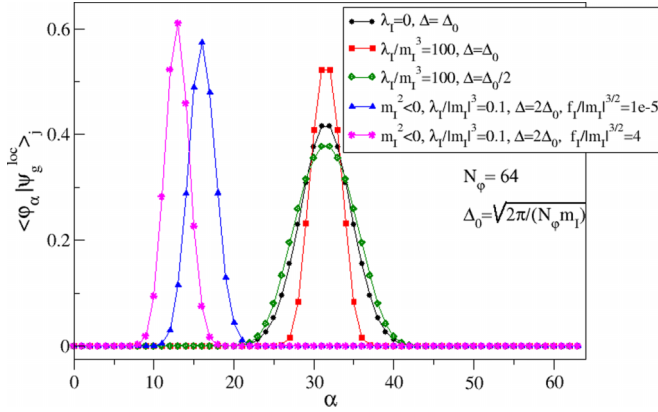


FIG. 2. Ground state wave functions, $\langle \varphi_\alpha | \psi_g^{\text{loc}} \rangle_j$, of the local Hamiltonian $H_{\text{loc},j}$ in Eq. (42) represented on $n_q = 6$ qubits ($N_\varphi = 64$) vs the discretization index $\alpha \in \{0, 1, \dots, N_\varphi - 1\}$ [see Eq. (11)]. The black circles illustrate the harmonic oscillator ground state ($\lambda_I = 0$), which is a Gaussian. The red squares (green diamonds) illustrate the anharmonic oscillator ground state with strong interaction, $\lambda_I/m_I^3 = 100$, for a chosen discretization interval $\Delta = \Delta_0 \equiv \sqrt{2\pi/(N_\varphi m_I)}$ ($\Delta = \Delta_0/2$). The blue triangles illustrate the ground state for the Hamiltonian with negative mass-squared and small external field. The magenta stars illustrate the ground state for the Hamiltonian with negative mass-squared and significant external field. These states are obtained by employing exact diagonalization.

made by successive one-qubit and two-qubit layers. A one-qubit layer consists of one $R^y(\theta_i)$ rotation followed by one $R^z(\theta_j)$ rotation on every qubit. A two-qubit layer, which is responsible for introducing entanglement, consists of CZ gates acting on neighboring qubits. Qubit pairing in successive entanglement layers differs from each other and alternates. The quantum state $|\phi_{qc}(\theta)\rangle$ depends on M rotation angles $\theta = (\theta_1, \dots, \theta_M)$ of the R^y and R^z single-qubit gates in the circuit. Since, typically, n_q is a small number (6–8), the state $|\phi_{qc}(\theta)\rangle$ can be computed on a classical computer without memory limitation problems, using packages such as `Cirq` [57] or `Qiskit` [58].

Third, the M rotation angles, θ , that parametrize the circuit are chosen so that the fidelity

$$F(\theta) = \left| \langle \phi_{qc}(\theta) | \psi_g^{\text{loc}} \rangle_j \right|^2 \quad (46)$$

is as close to 1 as possible. This can be accomplished, for example, by using the Covariance Matrix Adaptation Evaluation Strategy (CMA-ES) [59] for optimization on a classical computer. CMA-ES is an iterative, genetic algorithm that generates a population of solutions at each iteration. The covariance matrix, calculated from a population subset with the largest values of $F(\theta)$, determines the population of solutions considered at the next iteration. The algorithm terminates when the best $F(\theta)$ of the population stops improving. The most difficult problem we encounter during the optimization of $F(\theta)$ is trapping at points of local maxima. We find that this problem can be avoided when CMA-ES runs with a large population of solutions.

In Fig. 2 we show the ground states of the local Hamiltonian $H_{\text{loc},j}$ represented on $n_q = 6$ qubits for different

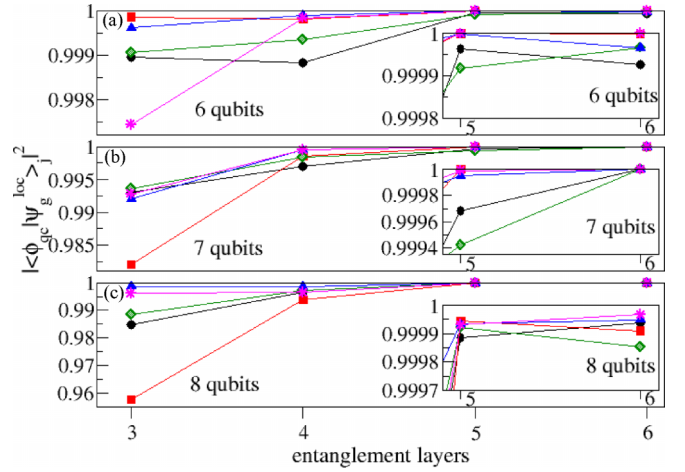


FIG. 3. (a) Fidelity of the quantum states illustrated in Fig. 2 (same legend) prepared using an optimized quantum circuit vs the number of circuit's entanglement layers. (b) The same as in (a) when the quantum states are represented on $n_q = 7$ qubits ($N_\varphi = 128$). (c) The same as in (a) when the quantum states are represented on $n_q = 8$ qubits ($N_\varphi = 256$). The fidelity generally increases with the number of entanglement layers of the variational circuit. However, the fidelity is not strictly monotonic since the circuit structure with an odd number of entanglement layer is different than that with an even number. For the cases with seven, seven, and eight qubits, the variational method reaches a fidelity > 0.9999 with six entanglement layers.

Hamiltonian parameters calculated using exact diagonalization. We are going to prepare these states by the parameterized circuits to demonstrate the efficiency of the variational preparation. For illustration, we have chosen parameters representing different regimes, such as noninteracting, strong interacting with positive squared mass, negative squared mass with small external field strength and negative squared mass with a significant external field strength. Since, as mentioned in Sec. III A and discussed at large in [39], the discretization interval Δ_φ in an interacting model can be tuned to optimize the performance of the algorithm, we present examples with $\Delta_\varphi = \sqrt{2\pi/(N_\varphi m_I)}$, $1/2\sqrt{2\pi/(N_\varphi m_I)}$, and $2\sqrt{2\pi/(N_\varphi m_I)}$. Note that the wave function representation on qubits depends significantly on Δ_φ . For example, the wave function plotted with red squares and the one plotted with green diamonds both correspond to the same Hamiltonian parameters $\lambda_I/m_I^3 = 100$ but the discretization interval of the latter is a factor of 2 smaller.

The state preparation fidelity of our parametrized circuits is shown in Fig. 3 as a function of entanglement layers, for $n_q = 6$, $n_q = 7$, and $n_q = 8$ qubits. The target states are the one illustrated in Fig. 2. For all examples, the fidelity of the local ground states is larger than 0.9999 when at least six entanglement layers are used. This is sufficient to accurately simulate a large lattice model. For example, the fidelity to prepare the local ground state of a lattice with $N = 100$ sites is estimated to be $0.9999^{100} \approx 0.99$, which is comparable to the typical two-qubit gate fidelity (~ 0.995) on NISQ devices [3–5]. If a higher fidelity is needed, more entanglement layers can be added to the variational circuit.

We do not encounter the difficulties seen in common variational quantum approaches such as the variational quantum eigensolver (VQE) [6,7] since the calculation of the quantum circuit required for state preparation is done on classical computers. We do not require a global minimum and any solution with high enough fidelity (i.e., larger than the target accuracy) is acceptable. The number of qubits n_q needed to prepare the local wave function is not very large. For example, $n_q = 8$ is enough even for the strong interacting regime, since it can accommodate ≈ 200 bosons per lattice site with great precision [39]. Hence, the barren plateau issue [42] is not a significant concern in our optimization. The optimization problem does not worsen when the system size is increased, since the optimized wave functions are local. For the preparation of an N -site lattice wave function $|\psi_g^{\text{loc}}\rangle$ [Eq. (44)], a quantum circuit running N parallel n_q quantum circuits should be used.

The variational circuit ansatz used here and constructed from R_Y , R_Z , and CZ gates is just a representative example. Different hardware-efficient circuit ansatzes can be employed. For example, the results of this section will be similar if one changes the CZ gate to the CNOT gate and the R_Y to the R_X .

B. Adiabatic evolution

Our state preparation method relies on the adiabatic theorem [60], which relates the ground state of the interacting ϕ^4 Hamiltonian H [Eq. (41)] to the ground state of the local Hamiltonian H_{loc} [Eq. (42)] under the action of the time-dependent Hamiltonian $H(s = t/T)$ [Eq. (45)] for a sufficiently long time T .

There is a vast literature [61] addressing the necessary and sufficient conditions the adiabatic time T should fulfill. A necessary condition is given by

$$T \gg \frac{1}{\epsilon} \max_{s \in [0,1]} |A_{m0}(s)| \quad \text{for all } m \neq 0, \quad \text{with} \quad (47)$$

$$A_{m0}(s) = \frac{\langle E_m(s) | \dot{E}_0(s) \rangle}{E_m(s) - E_0(s)}, \quad (48)$$

where $|E_m(s)\rangle$ is the m th instantaneous eigenstate of $H(s)$ satisfying $H(s)|E_m(s)\rangle = E_m(s)|E_m(s)\rangle$. The system starts evolving from $|E_0(0)\rangle \equiv |\psi_g^{\text{loc}}\rangle$. The dot denotes the derivative with respect to the s variable, $|\dot{E}_0(s)\rangle \equiv \frac{d}{ds}|E_0(s)\rangle$, and $\epsilon = \|U(1)|\psi_g^{\text{loc}}\rangle - |\psi_g^{\text{trg}}\rangle\|$ quantifies the difference between the state at the end of the the adiabatic evolution $U(1)|\psi_g^{\text{loc}}\rangle$ and the target state $|\psi_g^{\text{trg}}\rangle \equiv |E_0(1)\rangle$. Equation 47 is not a sufficient condition but provides a good estimate of T for a large number of problems [62,63]. The combination of this condition with the relation

$$\langle E_m(s) | \dot{E}_0(s) \rangle = \frac{\langle E_m(s) | \frac{dH(s)}{ds} | E_0(s) \rangle}{E_m(s) - E_0(s)} \quad \text{for } m \neq 0 \quad (49)$$

implies that T scales as the square of the minimum excitation gap. When the excitation gap along the evolution path vanishes, as it does when the system passes through a critical region, the adiabatic process fails.

The condition (47) is not always sufficient to ensure adiabatic evolution, typical examples where it fails being Hamiltonians with oscillatory terms. A further, necessary con-

dition for the validity of the adiabatic approximation [63] is given by

$$T \gg \frac{1}{\epsilon} \max_{s \in [0,1]} \left| \frac{d}{ds} A_{m0}(s) \right| \quad \text{for all } m \neq 0. \quad (50)$$

In our case, this second adiabatic condition is relevant for the preparation of the broken-symmetry state, as we will discuss in Sec. IV B 2.

The adiabatic time is shown to be proportional to the changing rate of the ground state wave function along the adiabatic path [64,65], i.e., $T \propto \int_0^1 ds \| |\dot{E}_0(s)\rangle \|$. Intuitively we expect that, the closer are the initial and the target wave functions, the smaller is the overall changing rate of the ground state along the path, and implicitly the required adiabatic time. In fact, for both normal and broken-symmetry phase preparations, we observe a direct correlation between the adiabatic time and the local overlap of the initial and the final wave functions. Namely, a larger overlap correlates with a shorter adiabatic time, as we discuss in Secs. IV B 1 and IV B 2.

The initial wave function is determined by the parameters m_I , λ_I and f_I . In the next sections we will explore the influence of these parameters on the adiabatic process. Since these parameters are adjustable in our algorithm, we will make recommendations for their choices.

The time dependence of the adiabatic process might significantly influence the adiabatic time. While for the preparation of normal phase states, we consider only adiabatic paths with linear time dependence, for the preparation of broken-symmetry states, we propose an adiabatic path with an exponential time dependence. This choice of the time dependence will mitigate the complications caused by the degeneracy of the ground state, as we discuss in Sec. IV B 2.

1. Preparation of normal phase states

Finding the optimal adiabatic path for adiabatic evolution is difficult without the knowledge of the system's excitation spectrum. However, our goal in this section is less ambitious, and consists in investigating the effect of the initial wave function $|\psi_g^{\text{loc}}\rangle$ [Eq. (44)] on the adiabatic process. For normal phase preparation we consider only adiabatic paths with linear time dependence, i.e., we take $\alpha(s) = s$ in Eq. (45).

The normal phase of the ϕ^4 model is characterized by a nondegenerate ground state. The symmetry-breaking external field is unnecessary for ground state preparation in this case, and we set $f_I = 0$ and $\delta f = 0$ in Eqs. (42) and (43). The dependence of $|\psi_g^{\text{loc}}\rangle$ on m_I and λ_I can be understood by writing the local Hamiltonian [Eq. (42)] as

$$\begin{aligned} \frac{H_{\text{loc},j}}{|m_I|} &= \frac{1}{2} \left(\frac{\Pi_j}{\sqrt{|m_I|}} \right)^2 + \text{sgn}(m_I^2) \frac{1}{2} (\sqrt{|m_I|} \Phi_j)^2 \\ &+ \frac{1}{4!} \frac{\lambda_I}{|m_I|^3} (\sqrt{|m_I|} \Phi_j)^4. \end{aligned} \quad (51)$$

Up to a field amplitude scaling factor $\sqrt{|m_I|}$ the eigenfunctions of $H_{\text{loc},j}$ are solely determined by the sign of m_I^2 and the ratio $\lambda_I/|m_I|^3$, while $|m_I|$ acts as a scaling factor for the energy.

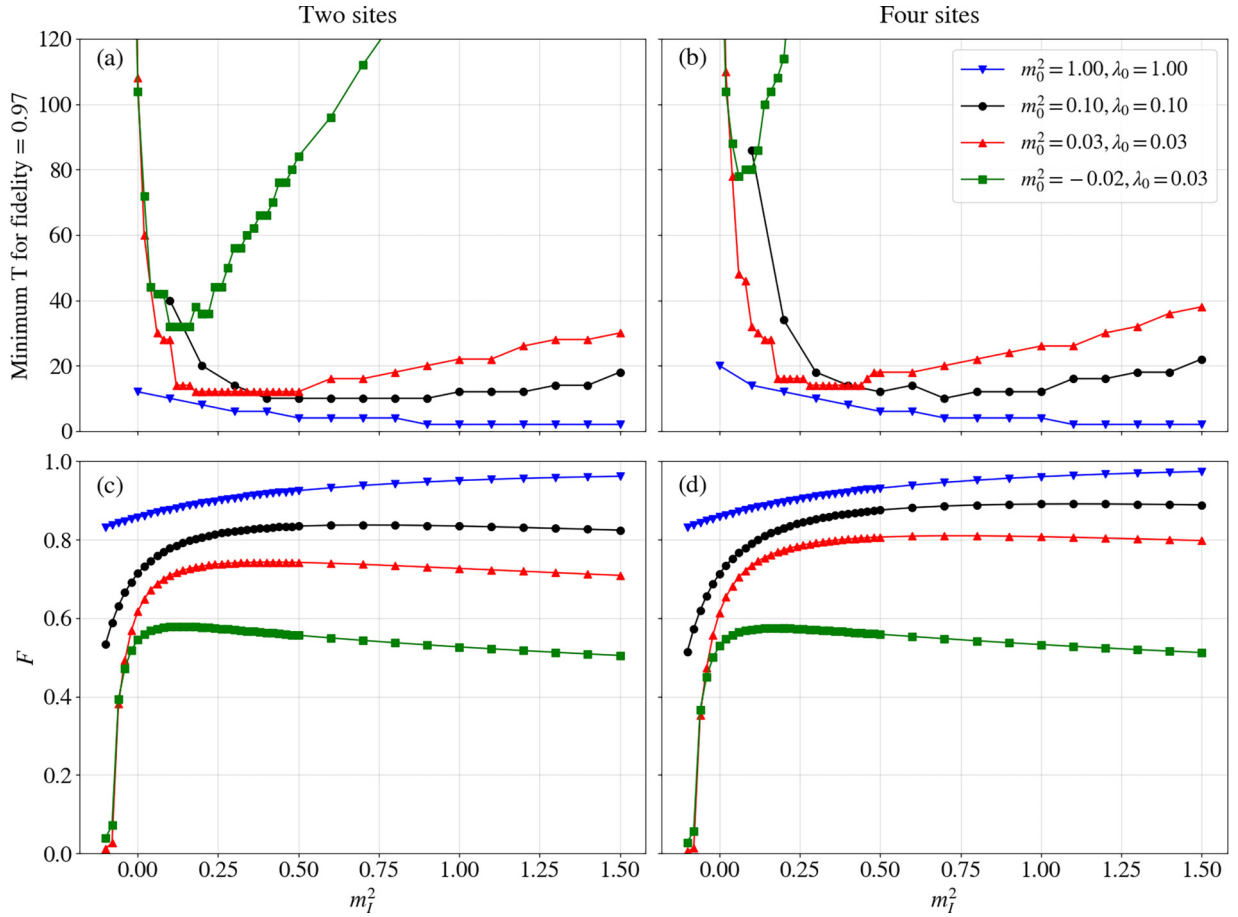


FIG. 4. Adiabatic time T required to prepare the ϕ^4 normal state with 0.97 fidelity vs m_l^2 for different values of the parameters m_0^2 and λ_0 for (a) two-site and (b) four-site lattices. T sensitivity on m_l^2 increases with decreasing m_0^2 . (c) and (d) Local fidelity F , Eq. (52), measuring the overlap of the initial and the final local density matrices, vs m_l^2 for two-site and, respectively, four-site lattices. The values of m_l^2 yielding the smallest T yield the largest F_{loc} . Note that the parameters and quantities displayed in this figure are dimensionless.

The adiabatic evolution on small lattices is simulated on classical computers, using the Trotterization method described in Sec. III C. We observe that m_l has a strong influence on the adiabatic time and there is an optimal value that minimizes the adiabatic time. Figures 4(a) and 4(b) show the adiabatic time T needed to prepare the ground state with 0.97 fidelity as a function of m_l^2 for different values of the dimensionless bare parameters m_0^2 and λ_0 for two- and four-site lattices. The value of T is especially sensitive to the mass parameter m_l when m_0 is small, a parameter regime relevant when taking the continuous limit $a \rightarrow 0$ (remember that $m_0 = m_b a$). We find that, in general, the optimal value of m_l^2 is larger than the bare mass m_0^2 .

The dependence of the adiabatic time on m_l can be understood by considering the strong influence of m_l on the initial wave function, since $\sqrt{|m_l|}$ acts as a scale factor for the field amplitude variable. Two competing effects come into play to determine the optimal m_l . On one hand, the initial gap increases with increasing m_l^2 , which favors the adiabatic process. On the other hand, increasing m_l^2 reduces the width of the initial wave function in the field amplitude basis. When the initial wave function is too narrow, significant changes of the wave function are required during evolution, which increases

the adiabatic time. In fact, for small lattices, we observe a direct correlation between the optimal adiabatic time and the local fidelity defined as [55]

$$F_{\text{loc}} = {}_j \langle \psi_g^{\text{loc}} | \rho_j | \psi_g^{\text{loc}} \rangle_j, \quad (52)$$

where $\rho_j = \prod_{k \neq j} \text{Tr}_k |\psi_g^{\text{trg}} \rangle \langle \psi_g^{\text{trg}}|$ is the reduced density matrix at site j of the system final ground state $|\psi_g^{\text{trg}} \rangle \equiv |E_0(s=1)\rangle$. In Eq. (52), Tr_k denotes the partial trace over a local basis at site k . The smallest T is obtained for the values of m_l^2 which yield the largest values of F_{loc} , as can be seen by comparing the top panel and bottom panel of Fig. 4.

Numerical simulations on small lattices reveal a weak dependence of the adiabatic time on the coupling strength λ_l used to prepare the initial state. Figure 5 shows the time T required to prepare the two- and four-site lattice ground state with fidelity 0.99 as a function of $\delta\lambda = \lambda_0 - \lambda_l$. The parameters m_0^2 and λ_0 chosen in these examples are small to accentuate the region where T is sensitive to m_l^2 . The chosen value of m_l^2 is close to the optimal one for $\delta\lambda = 0$. Particularly for the four-site lattice, the adiabatic time is nearly independent of λ_l .

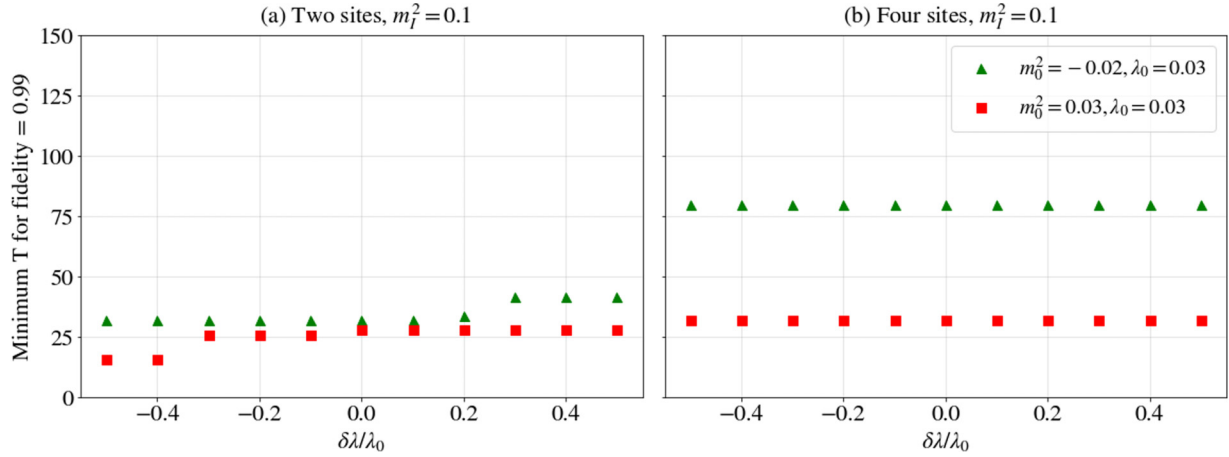


FIG. 5. Adiabatic time T as a function of $\delta\lambda$ for $m_l^2 = 0.1$, different values of the parameters m_0^2 and λ_0 for (a) two-site and (b) four-site lattices. The adiabatic time T dependence on $\delta\lambda = \lambda_0 - \lambda_l$ is weak. Note that the parameters and the adiabatic time T displayed in this figure are dimensionless.

2. Preparation of broken-symmetry states

Two issues related to the vanishing of the excitation gap must be addressed when preparing states in the broken-symmetry phase. One is the potential crossing of the critical region during adiabatic evolution. The other is the degeneracy of the broken-symmetry ground state. These problems can be overcome by introducing a time-dependent external field that couples to the scalar field during the adiabatic evolution. The linear term in the Hamiltonian breaks the symmetry $\phi \rightarrow -\phi$ and, hence, the degeneracy of the ground state. The field strength also controls the energy gap between the ground and first excited state. By dividing the adiabatic evolution into two steps, we can focus on and discuss the gap and degeneracy problems independently. The first adiabatic evolution starts from the ground state of the local Hamiltonian [Eq. (42)] and ends in the ground state of the full Hamiltonian with a finite external field. The second adiabatic evolution starts from the terminus of the first one and ends when the external field is brought to near vanishing values (of the order of the desired error). Our notation is such that the external field changes from f_l to f_M during the first stage of the evolution and from f_M to f_F in the second stage.

a. First adiabatic path: Avoiding the critical region ($f_l \rightarrow f_M$). Previous studies of quantum algorithms for ϕ^4 field theory [20] proposed state preparation via adiabatic evolution starting from the ground state of a noninteracting Hamiltonian. Since the noninteracting ground state belongs to the normal phase region of the phase diagram, preparing broken-symmetry states in this way implies crossing the critical region characterized by a vanishing excitation gap. This is problematic, since the adiabatic process requires a finite gap. Here we avoid crossing the critical region by starting the adiabatic evolution from a broken-symmetry state.

The first adiabatic path starts from a local state coupled to an external field f_l and ends in the ground state of the ϕ^4 model coupled to the external field f_M . The initial state is the ground state of Eq. (42) and is prepared variationally as described in Sec. IV A. The first adiabatic process here is described by Eq. (45) with linear time dependence, $\alpha(s) = s$,

and by Eq. (43) with $\delta f = f_M - f_l$. At the end of the first adiabatic path, the term containing the nonlocal coupling between sites is fully switched on. Since the ground state of the broken-symmetry phase of the ϕ^4 model in zero external field is doubly degenerate (or nearly double degenerate for finite size lattices) and well separated from the rest of the spectrum (as numerical simulations presented in Fig. 1 shows), f_M can be chosen small enough such that the low-energy spectrum of the system at the end of the first adiabatic path can be approximated by a coupled two-level system ($f_M |\sum_j \langle 0 | \Phi_j | 1 \rangle| \ll E_2 - E_1$, where E_1 and E_2 are the energies of the first and second excited states, respectively). This choice of f_M , while providing a significant gap during the first adiabatic path, will allow us to investigate analytically the second adiabatic process where the external field is taken to vanishing values.

Our goal is to develop an algorithm that minimizes the adiabatic time by varying the algorithm input parameters, i.e., the initial magnitude field f_l , the initial mass m_l^2 and the initial interaction strength λ_l . Similar to the normal phase preparation, we find that the adiabatic time remains correlated with the local overlap between the initial state at f_l and the intermediate state at f_M . In the following, we investigate the adiabatic time dependence on input parameters through numerical simulations of two, three, and four site lattices.

Simulations on small size lattices show that the shortest adiabatic times are correlated with the largest local overlap between the initial and final wave functions, similar to the normal-phase case discussed in Sec. IV B 1. An example is shown in Fig. 6 for the Hamiltonian parameters $m_0^2 = -0.22$, $\lambda_0 = 0.1$, and $f_M = 0.0011$. For this choice of the parameters, the coupling between sites [which is $1/2$ in the dimensionless units; see the first term in Eq. (43)] is the dominant term in the Hamiltonian. The parameter λ_l is fixed and equal to λ_0 . In Fig. 6(a) we show the adiabatic time required to reach the fidelity 0.97 while in Fig. 6(b) we show the local overlap, both as a function of m_l^2 and f_l . The correlation can be clearly observed in Fig. 6(c), where we plot the value of m_l^2 that yields the smallest T (red upper triangles) and the largest local overlap (blue upside down triangles) for a fixed f_l . In Fig. 6(d) we show the adiabatic time and local overlap versus f_l , with

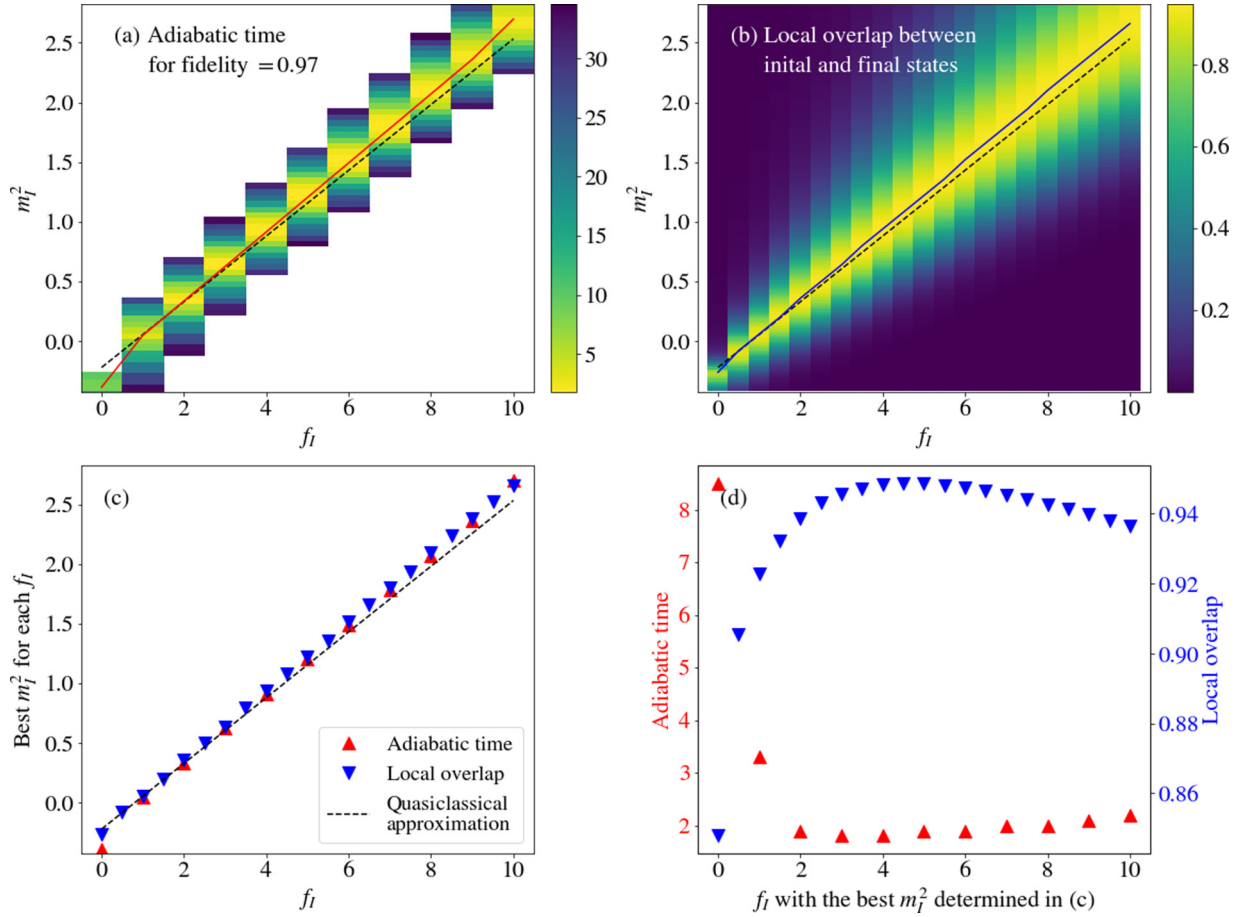


FIG. 6. Diagnostics on the adiabatic evolution algorithm: (a) Time T to reach a fidelity of 0.97 as a function of initial m_I^2 and external field strength; (b) the local overlap in the same coordinate space; (c) m_I^2 which minimizes the adiabatic time and maximizes the local overlap for fixed f_I vs f_I ; (d) adiabatic time T and the local overlap vs f_I for $m_I^2(f_I)$ minimizing T and extracted from (c). (Dimensionless parameters: $m_0^2 = -0.22$, $\lambda_0 = \lambda_I = 0.1$, $f_M = 0.0011$).

$m_I^2 = m_I^2(f_I)$ extracted from Fig. 6(c) to minimize T at fixed f_I . We find that for the optimal adiabatic time, the external field $f_I \gg f_M$ and the initial mass parameter $m_I^2 > 0 > |m_0^2|$. Similar investigations (with fixed λ_I) for other parameters of the Hamiltonian, including smaller m_0^2 and λ_0 lead to similar conclusions (not shown).

The relation between the local overlap (and implicitly of the adiabatic time) and the parameters m_I^2 and f_I can be understood by investigating the effect of these parameters on the initial wave function. The initial wave function's main peak position and the peak's width are dependent on both f_I and m_I^2 . In Fig. 7 we show the initial wave function distribution $|\langle \varphi_\alpha | \psi_g^{\text{loc}} \rangle_j|^2$ for different input parameters m_I^2 and f_I together with the local (at site j) probability distribution of the target wave function, defined as $p(\varphi)_j = \langle \varphi_\alpha | \rho_j | \varphi_\alpha \rangle$ [see Eq. (52) for the definition of ρ_j]. In the figure, the local field amplitude $|\varphi_\alpha\rangle$ is discretized to $N_\varphi = 32$ points, corresponding to using five qubits for each site. Figure 7(a) shows that the maximum overlap is obtained by choosing a value of $f_I \gg f_M$, in agreement with the plot shown in Fig. 6(d). The initial wave function with the largest local overlap (green crosses) with the target wave function is centered at the same location and has a similar width as the target wave function (black dots). By

increasing (decreasing) f_I while keeping m_I^2 fixed, the wave function peak moves to the left (right). If the initial mass m_I^2 is increased (decreased) such to keep the peak aligned with the target wave function's peak, the wave function distribution becomes too narrow (wide) compared to the target one, as illustrated with red squares (blue pluses). Consequently the overlap decreases. The case where the external field f_I is chosen small, comparable to f_M , is shown in Fig. 7(b). In this case, the local overlap is not optimal because the initial wave function exhibits a double-peak structure (green crosses and blue pluses).

An exhaustive, numerical search in a three dimensional space for the point (f_I, m_I, λ_I) which minimizes the adiabatic time is infeasible. Instead, we explore the adiabatic time dependence in the vicinity of the point $(f_{I0}, m_{I0}, \lambda_0)$, where f_{I0} and m_{I0} are the initial external field and initial mass parameter which yield the shortest adiabatic time when $\lambda_I = \lambda_0$, as described in the example shown in Fig. 6. We find that modifying λ_I in the vicinity this point does not reduce the adiabatic time. For example, in Fig. 8 we show results for Hamiltonian parameters $m_0^2 = -0.8$, $\lambda_0 = 0.6$, and $f_M = 0.001$. We keep $f_I = f_{I0} = 4.0008$ fixed and vary λ_I and m_I^2 . The adiabatic time and the local overlap as a function of λ_I/λ_0 and m_I^2

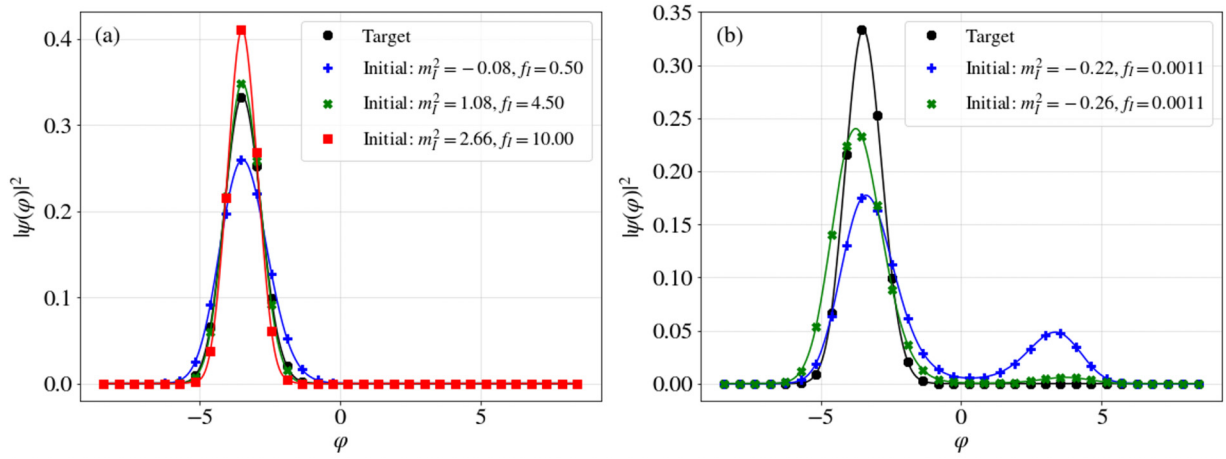


FIG. 7. Initial and target wave functions. The probability distribution along one of the field-amplitude coordinates (dimensionless) for different initial wave functions and the target wave function being the ground state of the full Hamiltonian. (a) m_I^2 dependence; (b) external field dependence. (Dimensionless parameters: $m_0^2 = -0.22$, $\lambda_0 = \lambda_I = 0.1$, $f_M = 0.0011$).

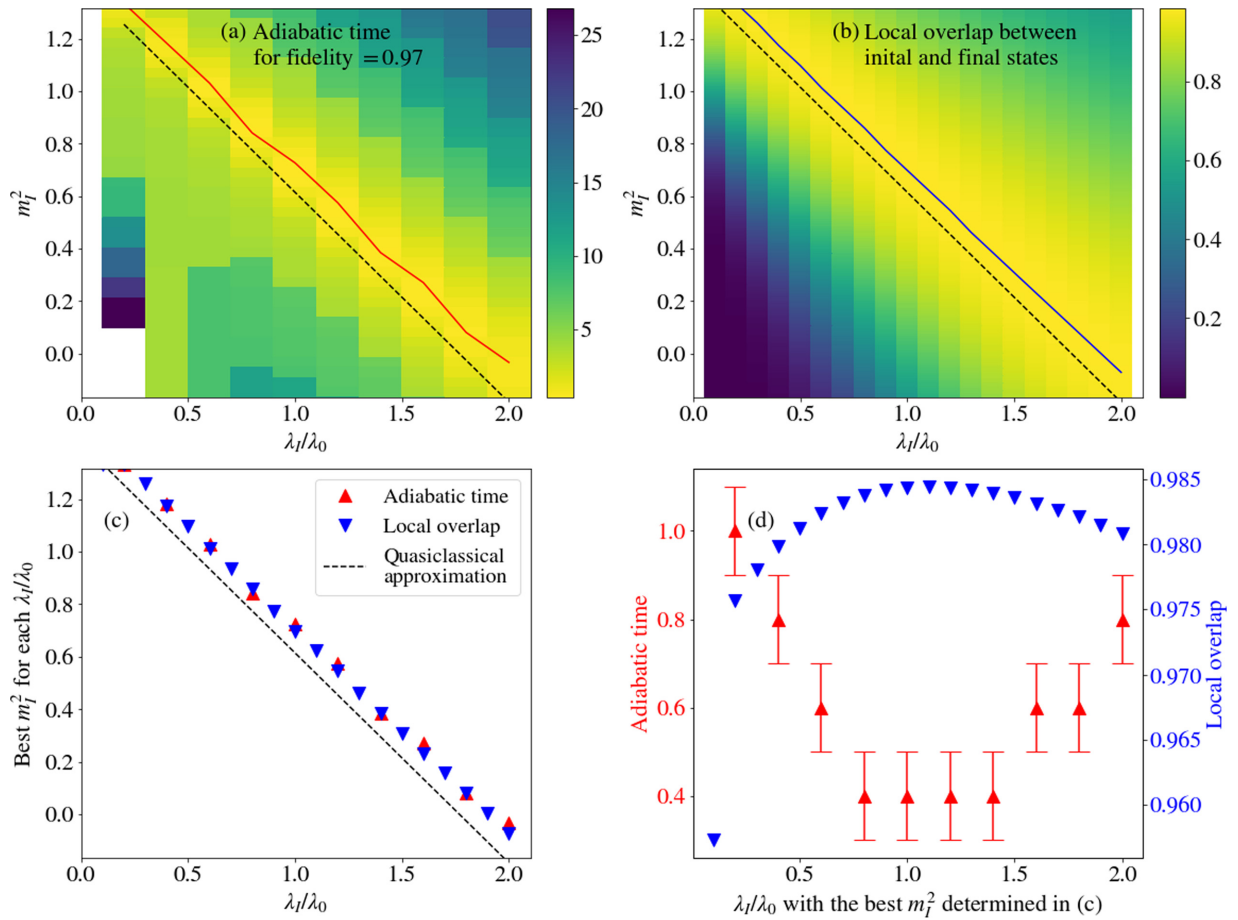


FIG. 8. Adiabatic evolution time and local overlap as a function of m_I^2 and λ_I when f_I is fixed to the value optimal for $\lambda_0 = \lambda_I$. (a) The time T to reach a fidelity of 0.97 as a function of input parameters m_I^2 and initial λ_I ; (b) the local overlap between the initial and the target wave function as a function of input parameters m_I^2 and initial λ_I ; (c) m_I^2 yielding the shortest T (red upper triangles) and the largest local overlap (blue upside down triangles) at fixed λ_I vs λ_I/λ_0 . (d) T and local overlap vs λ_I/λ_0 for $m_I = m_I(\lambda_I)$ yielding the shortest adiabatic time at fixed λ_I extracted from (c). The minimum adiabatic time and the maximum local overlap are found around $\lambda_I = \lambda_0$. (Dimensionless parameters: $m_0^2 = -0.8$, $\lambda_0 = 0.6$, $f_M = 0.0014$).

are shown in Figs. 8(a) and 8(b), respectively. The minimum adiabatic time correlates with the maximum local overlap as in the previous example, as can be seen from Fig. 8(c) where the m_I^2 which yields the shortest adiabatic time and m_I^2 which yields the largest local overlap for fixed λ_I are shown. While the adiabatic time dependence on λ_I is not negligible, we find that the shortest adiabatic time occurs when $\lambda_I \approx \lambda_0$, as can be seen in Fig. 8(d). Simulations for other Hamiltonian parameters (not shown), lead to the same conclusion: varying the input parameter λ_I in the vicinity of λ_0 does not decrease the adiabatic time.

In Figs. 6 and 8, it appears that there is a nearly linear relation between f_I and the corresponding best m_I^2 for both the adiabatic time and local overlap. This could be explained by the fact that, in this case, the local overlap is maximized when the potential energy minimum is the same for the initial and final Hamiltonians. An approximation of that relation can be obtained using the quasiclassical argument given in Appendix B and is shown as black dashed lines.

b. Ground state degeneracy ($f_M \rightarrow f_F$). The broken-symmetry phase of the ϕ^4 model is characterized by a twofold degenerate ground state in the thermodynamic limit and a nonzero value of the order parameter. In numerical simulations, the broken-symmetry ground state $|\psi_{a0}\rangle$ can be obtained from the ground state $|\psi_a(L, f)\rangle$ of a system of finite size L coupled to an external field f

$$H(f) = H + f \sum_{j=1}^N \Phi_j \quad (53)$$

by taking the limits

$$|\psi_{a0}\rangle = \lim_{f \rightarrow 0} \lim_{L \rightarrow \infty} |\psi_a(L, f)\rangle. \quad (54)$$

Equation 53 is the same as Eq. (7) with $f \equiv f_0$ and with the field operators replaced by the discrete field operators. The limiting order in Eq. (54) is important. When L is finite, the system in the absence of the external field is not truly degenerate. An arbitrary small external field can drive the system to a broken-symmetry state only after the limit $L \rightarrow \infty$. When estimating the limit Eq. (54) numerically, f should be decreased and L increased subject to the condition that $|f\langle 0 | \sum_j \Phi_j | 1 \rangle| \gg \Delta_0$, where the ground state of the system in zero external field is $|0\rangle$, the first excited state is $|1\rangle$, and the energy gap between them is $\Delta_0 = E_1 - E_0$.

The degeneracy of the ground state in the broken-symmetry phase is a problem for the adiabatic process, since the vanishing gap implies long adiabatic times. However, the quadratic adiabatic time scaling of the vanishing gap problem can be improved to linear by choosing an appropriate time dependence of the external field during the adiabatic process, as discussed in this section. We focus here on the adiabatic evolution in the vicinity of the final state characterized by vanishing external field. In this region, we assume that the nearly double degenerate ground state is well separated from the rest of the spectrum. The external field during our adiabatic process is always small such that the second term in Eq. (53) can be considered a small perturbation.

We denote the two low-energy states in the presence of the external field f by $|\psi_a(f)\rangle$ and $|\psi_b(f)\rangle$. As described in

Appendix C, a perturbative analysis reveals that the difference between the ground state of the system coupled to the external field f , $|\psi_a(f)\rangle$, and the broken-symmetry state, $|\psi_{a0}\rangle$, is

$$\| |\psi_a(f)\rangle - |\psi_{a0}\rangle \| = \frac{1}{2} f B + O(f^2), \quad (55)$$

where B , explicitly derived in Eq. (C34), is a quantity independent of f and dependent on the $\sum_j \Phi_j$ matrix elements coupling the low-energy and the high-energy states. The gap dependence on f is given by [see Eq. (C35)]

$$\Delta_{ba} \equiv E_b - E_a = 2fv + O(f^2), \quad (56)$$

where

$$v = |\langle \psi_{a0} | \sum_j \Phi_j | \psi_{a0} \rangle| \quad (57)$$

is equal to the order parameter in the broken-symmetry phase [see also Eq. (C15)]. The wave function dependence on f yields

$$\langle \psi_b(f) | \frac{d}{df} | \psi_a(f) \rangle = \frac{B}{2} + O(f), \quad (58)$$

as derived in Eq. (C36).

The adiabatic process starts from $|\psi_{\text{ini}}\rangle$, the ground state of Hamiltonian Eq. (53) with the external field $f(s=0) \equiv f_M$. At the end of the adiabatic evolution the external field is $f(s=1) \equiv f_F$. The error associated with the broken-symmetry state preparation is

$$\varepsilon = \| |U(1)|\psi_{\text{ini}}\rangle - |\psi_{a0}\rangle \|, \quad (59)$$

where $U(1)|\psi_{\text{ini}}\rangle$ is the adiabatically prepared state and $|\psi_{a0}\rangle$ is the broken-symmetry state (target state). There are two contributions to ε . The first one is caused by the finite value of the final external field, and using Eq. (55) is given by

$$\varepsilon_f = \| |\psi_a(f_F)\rangle - |\psi_{a0}\rangle \| = \frac{1}{2} f_F B, \quad (60)$$

where $|\psi_a(f_F)\rangle$ is the ground state of Hamiltonian Eq. (53) with $f = f_F$. The second contribution is the error of the adiabatic process defined as the difference between the adiabatically prepared state and the ground state when the external field is f_F ,

$$\varepsilon_{ad} = \| |U(1)|\psi_{\text{ini}}\rangle - |\psi_a(f_F)\rangle \|. \quad (61)$$

The triangle inequality implies that the total error [defined by Eq. (59)] is bounded by the sum of these two contributions

$$\varepsilon \leq \varepsilon_f + \varepsilon_{ad}. \quad (62)$$

The challenge to preparing the broken-symmetry state through adiabatic evolution can be understood by inspecting the adiabatic condition Eq. (47). Employing Eqs. (56) and (58) the term A_{10} reads

$$A_{10}(s) = \frac{B}{4v} \frac{1}{f} \frac{df}{ds}. \quad (63)$$

When $\frac{1}{f} \frac{df}{ds}$ is large, $|A_{10}|$ and, implicitly, the adiabatic time become large.

For example, a large adiabatic time, with quadratic dependence on accuracy, is required for an external field with linear time dependence

$$f(s) = f_M - \delta_f s, \quad (64)$$

where $\delta_f = f_M - f_F$. The magnitude of $A_{10}(s)$ at the end of the adiabatic process becomes

$$|A_{10}(s=1)| = \frac{B^2 \delta_f}{8v} \frac{1}{\varepsilon_f} = \frac{\varepsilon_{s=0}(\varepsilon_{s=0} - \varepsilon_f)}{\Delta_{s=0}} \frac{1}{\varepsilon_f}, \quad (65)$$

where $\Delta_{s=0} = 2f_M v$ is the initial gap of this adiabatic path and $\varepsilon_{s=0} = Bf_M/2$ is the difference between the initial state and the target state. If one naively employs Eq. (47) to estimate adiabatic time and assumes $\varepsilon_{ad} \approx \varepsilon_f \approx \varepsilon/2$, the adiabatic time reads $T \approx \frac{B^2 \delta_f}{8v} \frac{1}{\varepsilon_{ad} \varepsilon_f} \approx \frac{B^2 \delta_f}{2v} \frac{1}{\varepsilon^2}$. However, the second adiabatic condition Eq. (50), should also be considered for assessing the validity of the adiabatic approximation. In this case it predicts an even longer adiabatic time, $T \approx \frac{1}{\varepsilon_{ad}} \left| \frac{dA_{10}}{ds}(s=1) \right| = \frac{B^3 \delta_f^2}{16v \varepsilon_{ad} \varepsilon_f^2} \approx \frac{B^3 \delta_f^2}{2v \varepsilon^3}$, thus an adiabatic time scaling as $O(\varepsilon^{-3})$. Fortunately, in the perturbative region where the system can be reduced to a two level effective model, one can do better than employing the adiabatic conditions Eqs. (47) and (50) for estimating the adiabatic time. Analytical and numerical calculations, presented in Appendix C 3 a, find that the best adiabatic time is obtained when f_F is taken small such that $\varepsilon_f \ll \varepsilon_{ad} \approx \varepsilon$. In this case [see also Eq. (C61)]

$$T \approx \frac{\pi B^2 \delta_f}{16v} \frac{1}{\varepsilon^2} \approx \frac{\pi}{2} \frac{\varepsilon_{s=0}}{\Delta_{s=0}} (\varepsilon_{s=0} - \varepsilon_f) \frac{1}{\varepsilon^2}. \quad (66)$$

Thus, for an external field with linear time dependence the required adiabatic time scales as $O(\varepsilon^{-2})$. This is an increase by a factor of ε^{-1} when compared to systems with nonvanishing excitation gaps.

Since the excitation gap vanishes at the end of the adiabatic path, an external field time dependence which slows towards the end of the adiabatic evolution is expected to improve the adiabatic process. As Eq. (63) predicts, the adiabatic time does not blow up when $\frac{1}{f} \frac{df}{ds}$ is kept in bounds. For example, if the external field decreases exponentially, T scales as $O(\varepsilon^{-1} \ln[\varepsilon^{-1}])$, which is better than $O(\varepsilon^{-2})$ for a linearly decreasing field. Indeed, by choosing

$$f(s) = f_M \exp(-\gamma s), \text{ with } \gamma = \ln(f_M/f_F) = \ln(\varepsilon_{s=0}/\varepsilon_f), \quad (67)$$

one has

$$|A_{10}| = \gamma \frac{B}{4v} = \gamma \frac{\varepsilon_{s=0}}{\Delta_{s=0}}, \text{ and } \frac{d}{ds} A_{10} = 0. \quad (68)$$

The adiabatic conditions Eqs. (47) and (50) predict an adiabatic time $T \approx \varepsilon_{ad}^{-1} \ln(\varepsilon_f^{-1})$. Taking $\varepsilon_f \approx \varepsilon_{ad} \approx \varepsilon/2$ this implies $T \approx \varepsilon^{-1} \ln(\varepsilon^{-1})$. In fact, explicit analytical and numerical calculations for a two-level systems, presented in Appendix C 3 b, find that

$$T \approx \frac{B}{2v \varepsilon_{ad}} \ln \left(\frac{B f_F}{2 \varepsilon_f} \right) = 2 \frac{\varepsilon_{s=0}}{\Delta_{s=0} \varepsilon_{ad}} \ln \left(\frac{\varepsilon_{s=0}}{\varepsilon_f} \right). \quad (69)$$

For a desired accuracy ε , one can show that [see Eqs. (C73) and (C74)]

$$\frac{B}{2v \varepsilon} \ln \left(\frac{B f_F}{2 \varepsilon} \right) \leq T \leq \frac{B}{v \varepsilon} \ln \left(\frac{B f_F}{\varepsilon} \right). \quad (70)$$

Note that T depends on the ratio $B/v = 4\varepsilon_{s=0}/\Delta_{s=0}$. A small ratio B/v implies that the wave function's dependence

on the external field is much weaker than the gap's dependence on the external field. For the small size lattices explored here, we find that B/v is $\sim 10^{-2}$ [using the dimensionless units defining the Hamiltonian Eq. (7)] close to the critical region and is decreasing rapidly when moving further away from the critical region. We conclude that, for the adiabatic preparation of the broken-symmetry states, the farther away from the critical region the states are the smaller adiabatic time is needed.

3. Adiabatic evolution input parameters selection

Finding the optimal input parameters f_I , m_I^2 , and λ_I for the preparation of large size lattice states is challenging. We propose a strategy that avoids very long quantum circuits that are infeasible for limited-coherence near-term quantum hardware. First, determine the optimal input parameters for a small lattice, as discussed here. Then, use those values as the starting point in a search for the optimal input parameters in increasingly larger systems, guided by local overlap measuring. The local overlap can be obtained by employing the SWAP test method [66]. This strategy implies running multiple evolution circuits for systems smaller than the target one. However, the evolution time for these runs is close to optimal, implying relatively short circuits.

V. CONCLUSION

In this paper, we present a circuit implementation of the evolution operator of the ϕ^4 lattice Hamiltonian on a qubit quantum computer and an algorithm to prepare states in both the normal and broken-symmetry phases. The implementation is efficient in its use of resources and leverages the adjustable parameters of the problem to produce high fidelity states. It is suitable for near-term quantum computers.

The evolution operator is implemented using the Trotterization method. The scalar field is encoded on the qubits using the discretized field amplitude representation [39] and requires a small number of qubits per site, $n_q \approx 6-8$. This number of qubits is adequate for exponential precision in even the strongly interacting regimes. The required number of qubits and gates per Trotter step scale with the lattice size N . The most computationally expensive part of the evolution is the Trotter step associated with the ϕ^4 interaction, which requires a number of two-qubit gates proportional to $N n_q^4$.

Our state preparation combines a variational approach with adiabatic evolution. The ϕ^4 Hamiltonian is split into two parts: a local Hamiltonian consisting of a sum of local terms (*i.e.* uncoupled terms describing interaction at each site) and an intersite coupling Hamiltonian that is switched on adiabatically to restore the full Hamiltonian. The adiabatic process starts from the ground state of the local Hamiltonian, which is determined variationally.

The ground state of the local Hamiltonian is prepared with high fidelity using short quantum circuits. These quantum circuits consists of a few ($\lesssim 6$) two-qubit entangling layers (CZ in our example) and parameterized single-qubit gates. The circuit parameters are calculated on a classical computer by optimizing the overlap of the circuit final state and the local Hamiltonian ground state obtained from exact diagonaliza-

tion. Since the local Hamiltonian is a sum of uncoupled terms at each site, the circuit optimization problem is reduced to the optimization of a circuit with a small number of qubits ($n_q \approx 6-8$) and is independent of the lattice size.

The local Hamiltonian contains the ϕ^4 interaction and, for the preparation of the broken-symmetry phase, a coupling of the scalar field to an external field. The parameters defining the local Hamiltonian, the initial mass m_I , the initial interaction coupling λ_I and the initial external field f_I , constitute the input of our algorithm and can be adjusted. The system's Hamiltonian is restored by the adiabatic evolution. The initial parameters can be optimized to decrease the adiabatic time necessary to reach the full Hamiltonian ground state.

Our numerical investigation on small lattices finds a correlation between the adiabatic time and the local overlap of the final wave function and the initial wave function. To reduce the adiabatic time, the input parameters m_I , λ_I and f_I , should be chosen such that the final and the initial states have a maximum local overlap. For state preparation in the normal phase, we find a strong dependence of the adiabatic time on m_I^2 and a weak dependence on λ_I . In this case, the optimal m_I^2 is positive and larger than the ϕ^4 Hamiltonian mass parameter $|m_0|^2$. For state preparation in the broken-symmetry phase, we find that the optimal adiabatic time is achieved when the adiabatic process starts from the ground state of a local Hamiltonian with significant external field f_I and a positive input mass parameter m_I^2 .

The correlation between the adiabatic time and the local overlap allows us to use the overlap as a tool to optimize the initial parameters. We propose an iterative strategy for finding the optimal input parameters m_I , λ_I and f_I , starting with the optimal values for small lattices and adjusting them in increasingly larger systems by maximizing the local overlap.

There are two main challenges associated with the preparation of the broken-symmetry states that are addressed in this paper. The first is when the adiabatic evolution crosses the critical phase transition region for an initial state in the symmetric phase. The second is the vanishing gap of the double degenerate broken-symmetry phase. We avoid these challenges by coupling the system to an external field during the adiabatic evolution. We propose an adiabatic process consisting of two steps. In the first step, the adiabatic evolution starts from a broken-symmetry state prepared variationally by coupling the local Hamiltonian to a finite external field. During this step, the coupling term is switched on and the external field is decreased. During the second step, the external field is decreased to vanishing values. The error in the adiabatic process can be kept under control by choosing a linear decrease of the external field in the first step and an exponential decrease in the second step.

ACKNOWLEDGMENTS

A.M. is partially supported by the DOE/HEP QuantISED program grant of the theory consortium ‘‘Intersections of QIS and Theoretical Particle Physics’’ at Fermilab. A.C.Y.L. and S.M. are partially supported by the DOE/HEP QuantISED program grant ‘‘HEP Machine Learning and Optimization Go Quantum,’’ identification number 0000240323. This manuscript has been authored by Fermi Research Alliance,

LLC under Contract No. DE-AC02-07CH11359 with the U.S. Department of Energy, Office of Science, Office of High Energy Physics.

APPENDIX A: FOURIER TRANSFORM GATE

In this Appendix, we prove Eq. (25), which expresses the discrete Fourier transform gate \mathcal{F}_j in terms of the QFT gate and single-qubit rotations. We begin from the definition of the discrete Fourier operator in Eq. (13):

$$\mathcal{F}_j = \frac{1}{\sqrt{N_\varphi}} \sum_{\alpha, \beta=0}^{N_\varphi-1} e^{i \frac{2\pi}{N_\varphi} (\alpha - \frac{N_\varphi-1}{2})(\beta - \frac{N_\varphi-1}{2})} |\varphi_\alpha\rangle_j \langle \varphi_\beta|_j. \quad (\text{A1})$$

Expanding the phase factor and inserting the identity operator $\mathbb{1} = \sum_{\alpha=0}^{N_\varphi-1} |\varphi_\alpha\rangle_j \langle \varphi_\alpha|_j$ leads to

$$\begin{aligned} \mathcal{F}_j &= e^{i \frac{N_\varphi \delta^2}{2\pi}} \left(\sum_{\alpha=0}^{N_\varphi-1} e^{-i\delta\alpha} |\varphi_\alpha\rangle_j \langle \varphi_\alpha|_j \right) \\ &\times \left(\frac{1}{\sqrt{N_\varphi}} \sum_{\mu, \nu=0}^{N_\varphi-1} e^{i \frac{2\pi}{N_\varphi} \mu \nu} |\varphi_\mu\rangle_j \langle \varphi_\nu|_j \right) \\ &\times \left(\sum_{\beta=0}^{N_\varphi-1} e^{-i\delta\beta} |\varphi_\beta\rangle_j \langle \varphi_\beta|_j \right), \end{aligned} \quad (\text{A2})$$

where $\delta = \frac{(N_\varphi-1)\pi}{N_\varphi}$. The first line is a phase factor, and it is relevant if we would like to implement a control Fourier transform gate. The third line is a standard QFT gate [55]. The second and the fourth lines can be implemented as single-qubit z rotation gates similar to Eq. (28) such that

$$\begin{aligned} &e^{-i\delta\alpha} |\varphi_\alpha\rangle_j \langle \varphi_\alpha|_j \\ &= e^{-i\delta \sum_{q=0}^{n_q-1} \alpha_{qj} 2^{n_q-1-q}} |\varphi_\alpha\rangle_j \langle \varphi_\alpha|_j \\ &= e^{-i\delta \sum_{q=0}^{n_q-1} \frac{2\alpha_{qj}-1}{2} 2^{n_q-1-q}} e^{-i\delta \frac{N_\varphi-1}{2}} |\varphi_\alpha\rangle_j \langle \varphi_\alpha|_j \\ &= e^{-i \frac{N_\varphi \delta^2}{2\pi}} \prod_{q=0}^{n_q-1} e^{-i\delta \frac{\alpha_{qj}}{2} 2^{n_q-1-q}} \\ &= e^{-i\delta^2 \frac{N_\varphi \delta^2}{2\pi}} \prod_{q=0}^{n_q-1} R_{qj}^z(2^{n_q-1-q}\delta). \end{aligned} \quad (\text{A3})$$

In the second line of the above equation, we used the binary representation $\alpha_j = \sum_{q=0}^{n_q-1} \alpha_{qj} 2^{n_q-1-q}$ [Eq. (23)]. Rewriting Eq. (A2) with QFT and R^z gates, we arrive at Eq. (25):

$$\begin{aligned} \mathcal{F}_j &= e^{-i \frac{N_\varphi \delta^2}{2\pi}} \prod_{q=0}^{n_q-1} R_{qj}^z(2^{n_q-1-q}\delta) \text{QFT}_j \\ &\times \prod_{q=0}^{n_q-1} R_{qj}^z(2^{n_q-1-q}\delta). \end{aligned} \quad (\text{A4})$$

APPENDIX B: SEMICLASSICAL DERIVATION OF THE RELATION BETWEEN THE OPTIMAL INITIAL MASS AND THE OPTIMAL INITIAL EXTERNAL FIELD

Here we present a semiclassical argument to explain the nearly linear relation between the best m_I^2 and f_M shown in Figs. 6 and 8. The adiabatic preparation is optimized when the local overlap between the initial ground state of $H(s=0)$ and the final ground state of $H(s=1)$ is close to maximum. While we do not have an analytic form of the ground-state wave function to determine the local overlap, we can determine the minimum of the classical potential energy, which in our case approximately predicts the center of the wave function. Hence, we find that, when the minima of the initial potential energy and the final potential coincide, the adiabatic protocol is close to optimal. The potential energy along the adiabatic path is given by

$$V(s) = \sum_{j=1}^N \left[\frac{m_I^2 + s \delta m^2}{2} \Phi_j^2 + \frac{s}{2} \sum_{e=0}^d (\Phi_{j+e} - \Phi_j)^2 + \frac{\lambda_I + s \delta \lambda}{4!} \Phi_j^4 + (f_I + s \delta f) \Phi_j \right]. \quad (\text{B1})$$

Given $m_0^2 < 0$ and assuming translational symmetry, the minimum of the potential energy is determined by

$$\left. \frac{\partial V(s)}{\partial \Phi_j} \right|_{\Phi_j = \Phi_0(s)} = 0, \quad (\text{B2})$$

where $\Phi_0 = \Phi_1 = \dots = \Phi_{N-1} = \Phi_0(s)$ is the location of the minimum. By requiring the minimum to be at the same position in the beginning ($s=0$) and at the end ($s=1$), i.e., $\Phi_0(0) = \Phi_0(1)$, we can find a relation between m_I^2 and f_I as shown in Figs. 6 and 8 as black dashed lines. In particular the linear relation

$$f_I = \mp \sqrt{\frac{3! |m_0^2|}{\lambda_0}} \left(m_I^2 + \frac{\lambda_I}{\lambda_0} |m_0^2| \right) + O(f_M) \quad (\text{B3})$$

is a good approximation. We emphasize that while this approximated relation aligns with the observations we made in the numerical simulation, this does not mean that the system properties in the low-energy subspace can be explained by a semiclassical argument. At best, the semiclassical argument gives us an insight about where the wave function is confined by the semiclassical potential in the field-amplitude basis. The distribution and most of the properties of the wave function remain strongly influenced by quantum effects and cannot be inferred from the semiclassical potential.

APPENDIX C: ADIABATIC PREPARATION OF A BROKEN-SYMMETRY STATE IN AN EFFECTIVE TWO-LEVEL SYSTEM

In this Appendix, we investigate the adiabatic condition for the preparation of the broken-symmetry states near the end of the path in Sec. IV B 2 b. Using an effective two-level system to approximate a nearly degenerate subspace, we will derive the adiabatic condition and propose more efficient adiabatic paths.

We consider a finite system of size L in the parameter regime corresponding to the broken-symmetry phase. The two lowest energy states $|0\rangle$ and $|1\rangle$ are nearly degenerate and well separated from the rest of the spectrum,

$$\Delta_0 \equiv E_1 - E_0 \ll E_2 - E_1 \equiv \Delta_1. \quad (\text{C1})$$

In the thermodynamic limit, the states $|0\rangle$ and $|1\rangle$ are degenerate,

$$\Delta_0(L) \xrightarrow{L \rightarrow \infty} 0. \quad (\text{C2})$$

The broken-symmetry state can be reached by coupling the system to an external field

$$H_f = H + f\Phi, \quad \text{where} \quad (\text{C3})$$

$$\Phi = \sum_{j=1}^N \Phi_j, \quad (\text{C4})$$

and then taking the limits $L \rightarrow \infty$ followed by $f \rightarrow 0$. Perturbation theory can be applied in this limit. We then apply a Schrieffer-Wolff transformation [67] to obtain an effective two-level Hamiltonian.

1. Review of Schrieffer-Wolff transformation

In this subsection, we will provide a quick review of the Schrieffer-Wolff transformation. In general, we can separate the full Hamiltonian into the unperturbed part H and the leading-order perturbation Φ such that

$$H_f = H + f\Phi. \quad (\text{C5})$$

The unperturbed part H is twofold degenerate due to a double-well potential. We consider the nearly degenerate subspace to be spanned by the states $|0\rangle$ and $|1\rangle$, each localized at one of the potential wells with an energy $E_0(f=0)$.

We carry out the perturbative calculation in this subspace using a Schrieffer-Wolff transformation, which constructs an effective Hamiltonian $H_{\text{eff}} = e^{-S} H_f e^S$ decoupling the twofold degenerate subspace from the higher-energy eigenstates up to an arbitrary order of f . The generator S can be constructed iteratively using a canonical van Vleck formalism [67].

To derive our result, we separate Φ into a block diagonal piece V_D and a piece V_X that couples the degenerate subspace and the higher-energy subspace. The generator S has a series expansion

$$S = \sum_{j=1}^{\infty} f^j S^{(j)}. \quad (\text{C6})$$

Applying the Baker-Hausdorff lemma, we can expand the transformed Hamiltonian into

$$\begin{aligned} H_{\text{eff}} &= e^{-S} (H + fV_D) e^S + e^{-S} fV_X e^S \\ &= H' + [H + fV_D, S] + \frac{1}{2} [[H, S], S] \\ &\quad + fV_X + f[V_X, S] + O(f^3) \\ &= H + f(V_D + V_X + [H, S^{(1)}]) \\ &\quad + f^2 \left(\frac{1}{2} [[H, S^{(1)}], S^{(1)}] + [V_X, S^{(1)}] + [H, S^{(2)}] \right. \\ &\quad \left. + [V_D, S^{(1)}] \right) + O(f^3). \end{aligned} \quad (\text{C7})$$

To decouple the two subspaces, we pick

$$[H, S^{(1)}] = -V_X, \quad (\text{C8})$$

$$[H, S^{(2)}] = -[V_d, S^{(1)}]. \quad (\text{C9})$$

We can use the resolvent operator technique to determine the generator such that

$$S^{(1)}|m\rangle = -R_m[H, S^{(1)}]|m\rangle, \quad (\text{C10})$$

where the resolvent operator is given by

$$R_m = \sum_{n \neq m} \frac{|n\rangle\langle n|}{E_m - E_n}. \quad (\text{C11})$$

This gives

$$S^{(1)} = \sum_{k=0,1} \sum_{\gamma \geq 2} \left(\frac{\langle \gamma | V_X | k \rangle}{E_k - E_\gamma} |\gamma\rangle\langle k| - \frac{\langle k | V_X | \gamma \rangle}{E_k - E_\gamma} |k\rangle\langle \gamma| \right).$$

The effective Hamiltonian up to the second order is given by

$$H_{\text{eff}} = H + fV_D + f^2 \frac{1}{2} [V_X, S^{(1)}]. \quad (\text{C12})$$

In the nearly degenerate subspace, H_{eff} can be written as

$$H_{\text{eff}} = \sum_{j=0,1} E_j |j\rangle\langle j| + f \sum_{j,k=0,1} V_{jk} |j\rangle\langle k| + f^2 \sum_{j,k=0,1} W_{jk} |j\rangle\langle k| + O(f^3), \quad (\text{C13})$$

where $W_{jk} = \sum_{\gamma \geq 2} \frac{\langle j | \Phi | \gamma \rangle \langle \gamma | \Phi | k \rangle}{2} \left(\frac{1}{E_\gamma - E_0} + \frac{1}{E_\gamma - E_1} \right)$ and $V_{jk} = \langle j | \Phi | k \rangle$. The first two terms in the equation are simply the projection of $H + f\Phi$ in the nearly degenerate subspace. The last term comes from the perturbative treatment and can be understood as the virtual interaction between the two nearly degenerate states through the higher-energy states.

2. Effective two-level model

Ignoring the higher-order terms in Eq. (C13), we get

$$H_{\text{eff}} = \sum_{j=0,1} E_j |j\rangle\langle j| + f \sum_{j,k=0,1} V_{jk} |j\rangle\langle k| + f^2 \sum_{j,k=0,1} W_{jk} |j\rangle\langle k|. \quad (\text{C14})$$

Note that $V_{00} = 0$, and $V_{11} = 0$ since $|0\rangle$ and $|1\rangle$ have the full symmetry of the Hamiltonian H , while Φ breaks the Z_2 symmetry. For convenience we will denote

$$v = |V_{01}| = |V_{10}|. \quad (\text{C15})$$

The implicit assumption made when applying the perturbation theory is that f is small such that $fv \ll \Delta_1$. We also assume that the system is large such that $\Delta_0 \ll fv$. We ignore terms of $O(\Delta_0/[fv])$ in the following.

The effective Hamiltonian (C14) acts on the two-dimensional space spanned by the states $|0\rangle$ and $|1\rangle$. The following notation is convenient:

$$s = \frac{1}{2} [E_0 + E_1 + f^2(W_{00} + W_{11})], \quad (\text{C16})$$

$$\delta = \frac{1}{2} [\Delta_0 + f^2(W_{11} - W_{00})], \quad (\text{C17})$$

$$t = fV_{01} + f^2W_{01}, \quad (\text{C18})$$

$$D = \frac{\delta}{\sqrt{\delta^2 + |t|^2}}, \quad (\text{C19})$$

$$t = |t|e^{-i2f}, \quad (\text{C20})$$

$$\tan 2\theta = -\frac{|t|}{\delta}, \quad (\text{C21})$$

$$\cos^2 \theta = \frac{1}{2}(1 + D), \quad \cos \theta = \sqrt{\frac{1+D}{2}}, \quad (\text{C22})$$

$$\sin^2 \theta = \frac{1}{2}(1 - D), \quad \sin \theta = -\sqrt{\frac{1-D}{2}}. \quad (\text{C23})$$

The eigenstates of the Hamiltonian (C14) can be written as

$$|\psi_a(f)\rangle = e^{-if} \cos \theta |0\rangle + e^{if} \sin \theta |1\rangle, \quad (\text{C24})$$

$$|\psi_b(f)\rangle = -e^{-if} \sin \theta |0\rangle + e^{if} \cos \theta |1\rangle, \quad (\text{C25})$$

while the corresponding energies are

$$\mathcal{E}_a = s - \sqrt{\delta^2 + |t|^2}, \quad (\text{C26})$$

$$\mathcal{E}_b = s + \sqrt{\delta^2 + |t|^2}. \quad (\text{C27})$$

Defining the broken-symmetry states as

$$|\psi_{a0}\rangle = \lim_{f \rightarrow 0} |\psi_a(f)\rangle = \frac{1}{\sqrt{2}} (e^{-if} |0\rangle - e^{if} |1\rangle), \quad (\text{C28})$$

$$|\psi_{b0}\rangle = \lim_{f \rightarrow 0} |\psi_b(f)\rangle = \frac{1}{\sqrt{2}} (e^{-if} |0\rangle + e^{if} |1\rangle), \quad (\text{C29})$$

the eigenstates of the system can be written as

$$|\psi_a(f)\rangle = \frac{(\cos \theta - \sin \theta)}{\sqrt{2}} |\psi_{a0}\rangle + \frac{(\cos \theta + \sin \theta)}{\sqrt{2}} |\psi_{b0}\rangle, \quad (\text{C30})$$

$$|\psi_b(f)\rangle = -\frac{(\cos \theta + \sin \theta)}{\sqrt{2}} |\psi_{a0}\rangle + \frac{(\cos \theta - \sin \theta)}{\sqrt{2}} |\psi_{b0}\rangle. \quad (\text{C31})$$

The quantity D in Eq. (C19) can be written as

$$D = fB - f^2AB + O(f^3) + O\left(\frac{\Delta_0}{fv}\right), \quad (\text{C32})$$

where

$$A = \frac{(V_{01}W_{10} + V_{10}W_{01})}{2v^2}, \quad (\text{C33})$$

$$B = \frac{(W_{11} - W_{00})}{2v}, \quad (\text{C34})$$

are independent on the external field f . The following quantities, relevant for the investigation of the adiabatic process, can be written up to $O(f^3)$ and $O(\Delta_0/[fv])$ as

$$\Delta_{ba} = \mathcal{E}_b - \mathcal{E}_a = 2fv(1 + fA), \quad (\text{C35})$$

$$\begin{aligned} \langle \psi_b(f) | \frac{d}{df} | \psi_a(f) \rangle &= -\sin\theta \frac{d}{df} \cos\theta + \cos\theta \frac{d}{df} \sin\theta \\ &= \frac{1}{2}B - fAB + \frac{1}{4}f^2B^3 + O(f^3), \end{aligned} \quad (\text{C36})$$

$$\langle \psi_a(f) | \frac{d}{df} | \psi_b(f) \rangle = -\langle \psi_b(f) | \frac{d}{df} | \psi_a(f) \rangle, \quad (\text{C37})$$

$$||\langle \psi_a(f) \rangle - \langle \psi_{a0} \rangle|| = \frac{1}{2}D = \frac{1}{2}fB - \frac{1}{2}f^2AB. \quad (\text{C38})$$

3. Adiabatic evolution in a two-level system

Here we investigate the two-level system's evolution when the external field $f(s)$, depending on the variable $s = t/T$, changes during a time interval T from the initial value $f(s = 0) = f_i$ to the final value $f(s = 1) = f_f$. Note that this evolution corresponds to the second stage of the adiabatic process to prepare the broken-symmetry states in Sec. IV B 2 such that $f_i = f_M$ and $f_f = f_F$. The initial wave function is the ground state of the system when $f = f_i$, $|\psi_{\text{ini}}\rangle \equiv |\psi(s = 0)\rangle = |\psi_a(f_i)\rangle$. During the adiabatic evolution, the wave function is

$$|\psi(s)\rangle = c_a(s)|\psi_a[f(s)]\rangle + c_b(s)|\psi_b[f(s)]\rangle, \quad (\text{C39})$$

where $|\psi_a(f)\rangle$ and $|\psi_b(f)\rangle$ are the instantaneous eigenstates of the Hamiltonian (C14) with external field $f(s)$.

The state at the end of the adiabatic evolution is

$$|\psi_f\rangle \equiv |\psi(s = 1)\rangle = c_{af}|\psi_a(f_f)\rangle + c_{bf}|\psi_b(f_f)\rangle, \quad (\text{C40})$$

where we denote $c_{af} \equiv c_a(1)$ and $c_{bf} \equiv c_b(1)$. The adiabatic error is given by the difference between the system's state at the end of the adiabatic evolution and the ground state when $f = f_f$,

$$\begin{aligned} \epsilon_{ad} &= ||\langle \psi_f \rangle - \langle \psi_a(f_f) \rangle|| = \sqrt{2(1 - |c_{af}|^2)} \\ &\approx |c_{bf}| + O(|c_{bf}|^4). \end{aligned} \quad (\text{C41})$$

The error caused by the finite final field, defined as the difference between the eigenstate when $f = f_f$ and the broken-symmetry state, is obtained by applying Eq. (C38):

$$\epsilon_f \equiv ||\langle \psi_a(f_f) \rangle - \langle \psi_{a0} \rangle|| = \frac{1}{2}Bf_f + O(f^2). \quad (\text{C42})$$

Employing Eqs. (C30), (C31), and (C39), the adiabatically prepared state can be written as

$$\begin{aligned} |\psi_f\rangle &= \frac{\cos\theta_f(c_{af} - c_{bf}) - \sin\theta_f(c_{af} + c_{bf})}{\sqrt{2}} |\psi_{a0}\rangle \\ &+ \frac{\cos\theta_f(c_{af} + c_{bf}) + \sin\theta_f(c_{af} - c_{bf})}{\sqrt{2}} |\psi_{b0}\rangle, \end{aligned} \quad (\text{C43})$$

where $\cos\theta_f$ and $\sin\theta_f$ are given by Eqs. (C22) and (C23) when $f = f_f$. The total error for preparing the broken-symmetry state is

$$\epsilon \equiv ||\langle \psi_f \rangle - \langle \psi_{a0} \rangle|| \approx |c_{af}\epsilon_f + c_{bf}|. \quad (\text{C44})$$

The coefficients $c_a(s)$ and $c_b(s)$, which describe the adiabatic evolution, obey the differential equations

$$\frac{dc_a}{ds} = -c_b(s) \frac{df}{ds} \langle \psi_a(f) | \frac{d}{df} | \psi_b(f) \rangle e^{-iT \int_0^s \Delta_{ba}(u) du}, \quad (\text{C45})$$

$$\frac{dc_b}{ds} = -c_a(s) \frac{df}{ds} \langle \psi_b(f) | \frac{d}{df} | \psi_a(f) \rangle e^{iT \int_0^s \Delta_{ba}(u) du}, \quad (\text{C46})$$

with the initial conditions $c_a(0) = 1$ and $c_b(0) = 0$. These equations can be solved numerically. Next we will present results for different choices of the time dependence of f : (1) linear and (2) exponential.

a. Adiabatic evolution with linear dependence of the external field

In this scenario, the field's time dependence is

$$f(s) = f_i + (f_f - f_i)s = f_i - \delta_f s, \quad (\text{C47})$$

where $\delta_f = f_i - f_f$. Equations (C45) and (C46) reduce to

$$\frac{dc_a}{ds} = -\frac{B}{2}\delta_f e^{-iTv(2f_i s - \delta_f s^2)} c_b(s), \quad (\text{C48})$$

$$\frac{dc_b}{ds} = \frac{B}{2}\delta_f e^{iTv(2f_i s - \delta_f s^2)} c_a(s). \quad (\text{C49})$$

At the end of this section we will present the numerical solution to these equations. However, in order to have an analytical estimate of the error dependence on the adiabatic time we proceed first by considering some simplifying approximations. We will judge the accuracy of these approximations by comparing the approximate results with the exact numerical solution.

First, taking into account that $|1 - c_a(s)| \approx \epsilon_{ad}$, Eq. (C49) can be written as

$$\begin{aligned} c_b(1) &= \frac{B}{2}\delta_f \int_0^1 ds e^{iTv \int_0^s (f_i - \delta_f u) du} + O(\epsilon_{ad}^2) \\ &= \frac{B}{2}\delta_f \int_0^1 ds e^{-iTv\delta_f(-2\frac{f_i}{\delta_f}s + s^2)} + O(\epsilon_{ad}^2) \\ &= \frac{B}{2}\delta_f e^{iTv\frac{f_i^2}{\delta_f}} \int_0^1 ds e^{-iTv\delta_f(s - \frac{f_i}{\delta_f})^2} + O(\epsilon_{ad}^2) \\ &= \frac{B}{2}\delta_f e^{iTv\frac{f_i^2}{\delta_f}} \frac{1}{\sqrt{Tv\delta_f}} \int_{\sqrt{Tv\delta_f}\frac{f_i}{\delta_f}}^{\sqrt{Tv\delta_f}\frac{f_f}{\delta_f}} dy e^{-iy^2} + O(\epsilon_{ad}^2). \end{aligned} \quad (\text{C50})$$

The integral in Eq. (C50) can be expressed in terms of the error function $\text{Erf}(x)$, as

$$\begin{aligned} c_b(1) &= e^{i\frac{3}{4}\pi} \frac{B}{4} \sqrt{\frac{\pi\delta_f}{Tv}} e^{iTv\frac{f_i^2}{\delta_f}} \left[\text{Erf}\left(e^{i\frac{\pi}{4}} \sqrt{\frac{Tv}{\delta_f}} f_i\right) \right. \\ &\quad \left. - \text{Erf}\left(e^{i\frac{\pi}{4}} \sqrt{\frac{Tv}{\delta_f}} f_f\right) \right] + O(\epsilon^2). \end{aligned} \quad (\text{C51})$$

The error function expansion at small argument is

$$\text{Erf}(e^{i\frac{\pi}{4}} x) = \sqrt{\frac{2}{\pi}}(1 + i)x - \frac{2}{\sqrt{\pi}} e^{i\frac{3\pi}{4}} \frac{x^3}{3} + O(x^5), \quad (\text{C52})$$

while at large argument is

$$\text{Erf}(e^{i\frac{\pi}{4}}x) = 1 - e^{-ix^2} \frac{1-i}{\sqrt{2\pi}} \frac{1}{x} + O(x^{-3}). \quad (\text{C53})$$

We distinguish two cases.

Case I. The adiabatic time satisfies

$$\frac{\delta_f}{vf_f^2} \ll T \ll \frac{\delta_f}{vf_f^2}. \quad (\text{C54})$$

In this case, the first error function in Eq. (C51) has a large argument while the second one has a small argument. The adiabatic error is

$$\begin{aligned} \epsilon_{ad} &= |c_b(1)| \\ &\approx B \frac{\sqrt{\pi}}{4} \sqrt{\frac{\delta_f}{Tv}} \left(1 - \sqrt{\frac{2}{\pi}} \sqrt{\frac{Tv}{\delta_f}} f_f \right) + O\left(\frac{1}{T}\right) \\ &\approx B \frac{\sqrt{\pi}}{4} \sqrt{\frac{\delta_f}{Tv}} - B \frac{f_f}{2\sqrt{2}}. \end{aligned} \quad (\text{C55})$$

This implies

$$\left(\epsilon_{ad} + \frac{1}{\sqrt{2}} \epsilon_f \right)^2 = \frac{\pi B^2 \delta_f}{16Tv}, \quad (\text{C56})$$

and an adiabatic time scaling as

$$T \approx \frac{\pi B^2 \delta_f}{16v} \frac{1}{\left(\epsilon_{ad} + \frac{1}{\sqrt{2}} \epsilon_f \right)^2}. \quad (\text{C57})$$

Equation (C54) implies that this approximation is valid when

$$\frac{1}{4\left(\epsilon_{ad} + \frac{1}{\sqrt{2}} \epsilon_f \right)^2} \ll \frac{1}{\pi \epsilon_f^2}, \quad (\text{C58})$$

or equivalently when

$$\epsilon_f \ll \frac{2}{\sqrt{\pi} - \sqrt{2}} \epsilon_{ad} \approx 5.58 \epsilon_{ad}, \quad (\text{C59})$$

i.e., when the final external field is chosen small enough that

$$\epsilon \approx \epsilon_{ad} \gg \epsilon_f. \quad (\text{C60})$$

In this case, the required adiabatic time scales inversely proportionally with the squared accuracy,

$$T \approx \frac{\pi B^2 \delta_f}{16v} \frac{1}{\epsilon^2}. \quad (\text{C61})$$

Case II. The adiabatic time satisfies

$$T \gg \frac{\delta_f}{vf_f^2} = \frac{\delta_f B^2}{4\epsilon_f^2}. \quad (\text{C62})$$

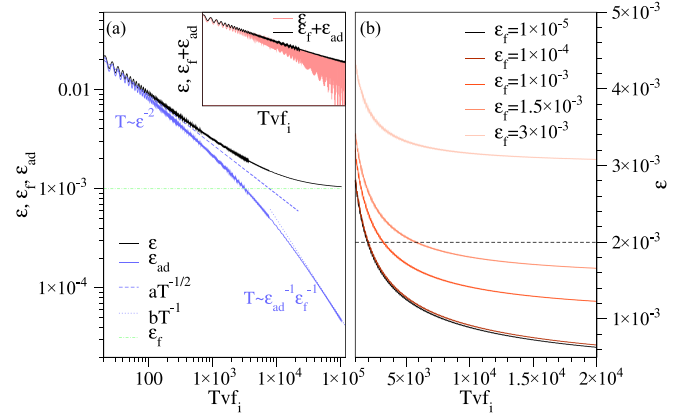


FIG. 9. Errors for preparing the broken-symmetry state when the external field has a linear time dependence in a two-level system with $B = 0.2$, $v = 10$, and $f_i = 1$. (a) Logarithmic scale. Errors ϵ , ϵ_f and ϵ_{ad} vs the adiabatic time T when $\epsilon_f = f_f B/2 = 10^{-3}$. The constants $a = B/4\sqrt{\pi}\delta_f/v$ and $b = \delta_f B^2/(8v\epsilon_f)$, see Eq. (C61) and, respectively, Eq. (C64). Inset: The error ϵ (light red line) has an oscillatory component as a function of T . The points of maximum are well approximated by $\epsilon_f + \epsilon_{ad}$ (black line). (b) The total error ϵ vs T for different choices of the final external field $f_f = 2\epsilon_f/B$. The adiabatic time for a fixed ϵ decreases with decreasing ϵ_f . The optimal adiabatic time is obtained in the parameter region where $\epsilon_f \ll \epsilon \approx \epsilon_{ad}$. Note that the parameters and quantities displayed are dimensionless.

In this case, both error functions appearing in Eq. (C51) have a large argument. The adiabatic error can be approximated by

$$\epsilon_{ad} = |c_b(1)| \approx \frac{\delta_f B}{4Tv f_f} = \frac{\delta_f B^2}{8Tv \epsilon_f}, \quad (\text{C63})$$

which implies

$$T \approx \frac{\delta_f B^2}{8v \epsilon_f \epsilon_{ad}}. \quad (\text{C64})$$

Equation (C62) implies that this approximation is valid when

$$\epsilon_f \gg \epsilon_{ad}. \quad (\text{C65})$$

Making the assumption (numerically verified) that both ϵ_f and ϵ_{ad} are independent and the total error is the sum of these two contributions, $\epsilon = \epsilon_f + \epsilon_{ad}$, one gets

$$T > \frac{\delta_f B^2}{2v \epsilon^2}. \quad (\text{C66})$$

By comparing the adiabatic time estimates for the two cases, Eqs. (C61) and (C64), one concludes that, for a desired accuracy ϵ , the choice of a large final external field (when $\epsilon \approx \epsilon_f \gg \epsilon_{ad}$) requires a larger T than the choice of a small final external field (when $\epsilon \approx \epsilon_{ad} \gg \epsilon_f$).

The errors calculated by solving Eqs. (C48), and (C49) numerically are shown in Fig. 9. Since the right hand side of these differential equations contains imaginary terms, the coefficients $c_{af}(T)$ and $c_{bf}(T)$ have an oscillatory component. As a consequence, ϵ and ϵ_{ad} display an oscillatory behavior, as can be seen from the inset. For our analysis of the numerical data, we consider the points where $\epsilon(T)$ reaches a

local maxima. As shown in the inset, $\epsilon \approx \epsilon_f + \epsilon_{ad}$ at these points, i.e., the adiabatic error and the final field error can be considered as independent contributions to the total error. In Fig. 9(a) we show the errors ϵ , ϵ_f and ϵ_{ad} dependence on T for a case where the final external field yields $\epsilon_f = 10^{-3}$. The numerical results are in agreement with the analytical analysis discussed earlier. At small T , where $\epsilon_{ad} \gg \epsilon_f$ the adiabatic time scales as $T \propto \epsilon^{-2}$, as predicted by Eq. (C61). At larger T where $\epsilon_{ad} \ll \epsilon_f$ the adiabatic time scales as $T \propto \epsilon_f^{-1} \epsilon_{ad}^{-1}$, as predicted by Eq. (C64).

In Fig. 9(b) we show the total error ϵ versus T for different values of the final external field. As our analytical analysis predicts, for a given ϵ (see, for example, the dashed black line) the required adiabatic time decreases with decreasing ϵ_f .

To conclude, we find that for an adiabatic process with linear time dependence of the external field, the adiabatic time scales as ϵ^{-2} .

b. Adiabatic evolution with exponential dependence of the external field

In this scenario, the external field's time dependence is

$$f(s) = f_i e^{-\gamma s} \quad \text{with } \gamma = \ln \frac{f_i}{f_f}. \quad (\text{C67})$$

Equations (C45) and (C46) reduce to

$$\frac{dc_a}{ds} = -\frac{1}{2} \gamma f B e^{-i\frac{2Tv}{\gamma}(f_i-f)} c_b(s), \quad (\text{C68})$$

$$\frac{dc_b}{ds} = \frac{1}{2} \gamma f B e^{i\frac{2Tv}{\gamma}(f_i-f)} c_a(s). \quad (\text{C69})$$

Employing the approximation $|1 - c_a(s)| \approx \epsilon_{ad}$, one has

$$\begin{aligned} c_b(1) &\approx -\frac{1}{2} B \gamma \int_0^1 ds f(s) e^{i2Tv \int_0^s f(u) du} + O(\epsilon_{ad}^2) \\ &= \frac{iB\gamma}{4Tv} (e^{i2Tv \int_0^1 f(s) ds} - 1) + O(\epsilon_{ad}^2) \\ &= \frac{iB\gamma}{4Tv} (e^{i\frac{2Tv\delta_f}{\gamma}} - 1) + O(\epsilon_{ad}^2). \end{aligned} \quad (\text{C70})$$

As for the linear adiabatic path case, $c_b(1)$ as a function of T has an oscillatory behavior. For the T values which yield local maxima of $|c_b(1)|$ [$T = (2k+1)\pi\gamma/(2v\delta_f)$, with k integer] the adiabatic error is

$$\epsilon_{ad} = |c_b(1)| \approx \frac{B\gamma}{2Tv}, \quad (\text{C71})$$

implying

$$T \approx \frac{B}{2v} \frac{1}{\epsilon_{ad}} \ln \frac{f_i}{f_f} = \frac{B}{2v} \frac{1}{\epsilon_{ad}} \ln \frac{Bf_i}{2\epsilon_f}. \quad (\text{C72})$$

Since $\epsilon_f, \epsilon_{ad} \leq \epsilon$, a lower bound for T is

$$T > \frac{B}{2v\epsilon} \ln \frac{Bf_i}{2\epsilon}. \quad (\text{C73})$$

For a desired accuracy ϵ , it is possible to determine the optimal ϵ_f and ϵ_{ad} which minimize T numerically. To find

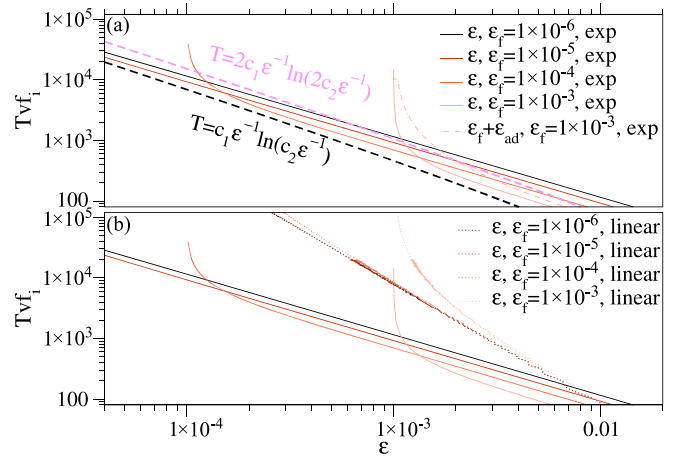


FIG. 10. Adiabatic time to prepare the broken-symmetry state in a two-level system with $B = 0.2$, $v = 10$ and $f_i = 1$. (a) External field with exponential time dependence. T vs ϵ for different values of the final external field $f = 2\epsilon_f/B$. When $\epsilon \gg \epsilon_f$, $T \approx \epsilon^{-1} \ln(\epsilon_f^{-1})$ in agreement with Eq. (C72). The approximation $\epsilon \approx \epsilon_f + \epsilon_{ad}$ does not hold well when ϵ approaches ϵ_f , but the bounds for the adiabatic time given by Eq. (C73) and Eq. (C74) are valid (see dashed lines where $c_1 = B/(2v)$ and $c_2 = Bf_i/2$). (b) Adiabatic time for the exponential path [solid lines, same legend as in (a)] and for the linear path (dotted lines) vs accuracy. The adiabatic time for the exponential path scales as $\epsilon^{-1} \ln \epsilon^{-1}$ which is better than the ϵ^{-2} scaling for the linear path. Note that the parameters and quantities displayed in this figure are dimensionless.

an asymptotic estimate for T , we assume ϵ_f and ϵ_{ad} are independent contributions to the total error, $\epsilon \approx \epsilon_f + \epsilon_{ad}$. Then the optimal T is smaller than or equal to the one obtained for $\epsilon_f = \epsilon_{ad} \approx \epsilon/2$,

$$T \leq \frac{B}{v\epsilon} \ln \frac{Bf_i}{\epsilon}. \quad (\text{C74})$$

The bounds provided by Eqs. (C73) and (C74) show that the time required for adiabatic evolution scales as

$$T \propto \frac{1}{\epsilon} \ln \frac{1}{\epsilon}, \quad (\text{C75})$$

which is an improvement compared to using an external field with linear time dependence, where $T \approx \epsilon^{-2}$ [see Eq. (C61)].

The results obtained by solving the differential equations (C68) and (C69) numerically are shown in Fig. 10(a). The adiabatic time satisfies Eq. (C72). The approximation $\epsilon \approx \epsilon_f + \epsilon_{ad}$ does not hold well in the region where ϵ approaches ϵ_f (see the solid and dash-dotted lines with the lightest color corresponding to $\epsilon_f = 10^{-3}$). However, the inequalities (C73) and (C74) are true. In Fig. 10(b) we compare the adiabatic time for the linear adiabatic path (dotted lines) with the one corresponding to the exponential adiabatic path (solid lines). As Eqs. (C61), and (C75) predict, the adiabatic time for the exponential case is much smaller than that for the linear case.

- [1] J. Preskill, *Quantum* **2**, 79 (2018).
- [2] A. J. Daley, I. Bloch, C. Kokail, S. Flannigan, N. Pearson, M. Troyer, and P. Zoller, *Nature (London)* **607**, 667 (2022).
- [3] M. Reagor, C. B. Osborn, N. Tezak, A. Staley, G. Prawiroatmodjo, M. Scheer, N. Alidoust, E. A. Sete, N. Didier, M. P. da Silva *et al.*, *Sci. Adv.* **4**, eaao3603 (2018).
- [4] F. Arute, K. Arya, R. Babbush, D. Bacon, J. C. Bardin, R. Barends, R. Biswas, S. Boixo, F. G. S. L. Brandao, D. A. Buell *et al.*, *Nature* **574**, 505 (2019).
- [5] P. Jurcevic, A. Javadi-Abhari, L. S. Bishop, I. Lauer, D. F. Bogorin, M. Brink, L. Capelluto, O. Günlük, T. Itoko, N. Kanazawa *et al.*, *Quantum Sci. Technol.* **6**, 025020 (2021).
- [6] P. J. J. O'Malley, R. Babbush, I. D. Kivlichan, J. Romero, J. R. McClean, R. Barends, J. Kelly, P. Roushan, A. Tranter, N. Ding *et al.*, *Phys. Rev. X* **6**, 031007 (2016).
- [7] A. Kandala, A. Mezzacapo, K. Temme, M. Takita, M. Brink, J. M. Chow, and J. M. Gambetta, *Nature (London)* **549**, 242 (2017).
- [8] C. Hempel, C. Maier, J. Romero, J. McClean, T. Monz, H. Shen, P. Jurcevic, B. P. Lanyon, P. Love, R. Babbush *et al.*, *Phys. Rev. X* **8**, 031022 (2018).
- [9] J. I. Colless, V. V. Ramasesh, D. Dahlen, M. S. Blok, M. E. Kimchi-Schwartz, J. R. McClean, J. Carter, W. A. de Jong, and I. Siddiqi, *Phys. Rev. X* **8**, 011021 (2018).
- [10] A. Kandala, K. Temme, A. D. Córcoles, A. Mezzacapo, J. M. Chow, and J. M. Gambetta, *Nature (London)* **567**, 491 (2019).
- [11] Google AI Quantum and Collaborators, F. Arute, K. Arya, R. Babbush, D. Bacon, J. C. Bardin, R. Barends, S. Boixo, M. Broughton, B. B. Buckley *et al.*, *Science* **369**, 1084 (2020).
- [12] A. Macridin, P. Spentzouris, J. Amundson, and R. Harnik, *Phys. Rev. Lett.* **121**, 110504 (2018).
- [13] A. Macridin, P. Spentzouris, J. Amundson, and R. Harnik, *Phys. Rev. A* **98**, 042312 (2018).
- [14] M. Gluza, M. Kliesch, J. Eisert, and L. Aolita, *Phys. Rev. Lett.* **120**, 190501 (2018).
- [15] H. Ma, M. Govoni, and G. Galli, *npj Comput Mater* **6**, 1 (2020).
- [16] A. Uvarov, J. D. Biamonte, and D. Yudin, *Phys. Rev. B* **102**, 075104 (2020).
- [17] W. Ji, L. Zhang, M. Wang, L. Zhang, Y. Guo, Z. Chai, X. Rong, F. Shi, X.-J. Liu, Y. Wang, and J. Du, *Phys. Rev. Lett.* **125**, 020504 (2020).
- [18] A. Roggero, A. C. Y. Li, J. Carlson, R. Gupta, and G. N. Perdue, *Phys. Rev. D* **101**, 074038 (2020).
- [19] A. Roggero, C. Gu, A. Baroni, and T. Papenbrock, *Phys. Rev. C* **102**, 064624 (2020).
- [20] S. P. Jordan, K. S. M. Lee, and J. Preskill, *Science* **336**, 1130 (2012).
- [21] N. Klco, E. F. Dumitrescu, A. J. McCaskey, T. D. Morris, R. C. Pooser, M. Sanz, E. Solano, P. Lougovski, and M. J. Savage, *Phys. Rev. A* **98**, 032331 (2018).
- [22] J. S. Pedernales, M. Beau, S. M. Pittman, I. L. Egusquiza, L. Lamata, E. Solano, and A. del Campo, *Phys. Rev. Lett.* **120**, 160403 (2018).
- [23] J. Hu, L. Feng, Z. Zhang, and C. Chin, *Nat. Phys.* **15**, 785 (2019).
- [24] H. Lamm, S. Lawrence, and Y. Yamauchi (NuQS Collaboration), *Phys. Rev. D* **100**, 034518 (2019).
- [25] T. Farrelly and J. Streich, Discretizing quantum field theories for quantum simulation, [arXiv:2002.02643](https://arxiv.org/abs/2002.02643) [quant-ph] (2020).
- [26] N. Klco and M. J. Savage, *Phys. Rev. A* **102**, 012612 (2020).
- [27] J. Barata, N. Mueller, A. Tarasov, and R. Venugopalan, *Phys. Rev. A* **103**, 042410 (2021).
- [28] M. Aizenman, *Phys. Rev. Lett.* **47**, 1 (1981).
- [29] J. Fröhlich, *Nucl. Phys. B* **200**, 281 (1982).
- [30] S.-J. Chang, *Phys. Rev. D* **13**, 2778 (1976).
- [31] S. F. Magruder, *Phys. Rev. D* **14**, 1602 (1976).
- [32] T. Sugihara, *J. High Energy Phys.* **05** (2004) 007.
- [33] A. Milsted, J. Haegeman, and T. J. Osborne, *Phys. Rev. D* **88**, 085030 (2013).
- [34] M. C. Bañuls and K. Cichy, *Rep. Prog. Phys.* **83**, 024401 (2020).
- [35] D. Schaich and W. Loinaz, *Phys. Rev. D* **79**, 056008 (2009).
- [36] P. Bosetti, B. De Palma, and M. Guagnelli, *Phys. Rev. D* **92**, 034509 (2015).
- [37] D. Lee, N. Salwen, and D. Lee, *Phys. Lett. B* **503**, 223 (2001).
- [38] S. Rychkov and L. G. Vitale, *Phys. Rev. D* **91**, 085011 (2015).
- [39] A. Macridin, A. C. Y. Li, S. Mrenna, and P. Spentzouris, *Phys. Rev. A* **105**, 052405 (2022).
- [40] A. Kitaev and W. A. Webb, [arXiv:0801.0342](https://arxiv.org/abs/0801.0342) (2008).
- [41] J. Liu, Z. Li, H. Zheng, X. Yuan, and J. Sun, *Mach. Learn. Sci. Technol.* **3**, 045030 (2022).
- [42] J. R. McClean, S. Boixo, V. N. Smelyanskiy, R. Babbush, and H. Neven, *Nat. Commun.* **9**, 4812 (2018).
- [43] H. F. Trotter, *Proc. Amer. Math. Soc.* **10**, 545 (1959).
- [44] M. Suzuki, *Commun. Math. Phys.* **51**, 183 (1976).
- [45] S. Lloyd, *Science* **273**, 1073 (1996).
- [46] S. P. Jordan, K. S. M. Lee, and J. Preskill, *Quant. Inf. Comput.* **14**, 1014 (2014).
- [47] M. Lüscher and P. Weisz, *Nucl. Phys. B* **290**, 25 (1987).
- [48] B. Freedman, P. Smolensky, and D. Weingarten, *Phys. Lett. B* **113**, 481 (1982).
- [49] I. Fox and I. Halliday, *Phys. Lett. B* **159**, 148 (1985).
- [50] C. Lang, in *Advances in Lattice Gauge Theory* (World Scientific Publishing, Singapore, 1985), pp. 25–60.
- [51] I. Drummond, S. Duane, and R. Horgan, *Nucl. Phys. B* **280**, 25 (1987).
- [52] A. Ciavarella, N. Klco, and M. J. Savage, *Phys. Rev. D* **103**, 094501 (2021).
- [53] M. S. Alam, S. Hadfield, H. Lamm, and A. C. Y. Li (SQMS Collaboration), *Phys. Rev. D* **105**, 114501 (2022).
- [54] E. J. Gustafson, H. Lamm, F. Lovelace, and D. Musk, *Phys. Rev. D* **106**, 114501 (2022).
- [55] M. A. Nielsen and I. Chuang, *Quantum Computation and Quantum Information* (Cambridge University Press, New York, 2002), pp. 216–221, 409.
- [56] J. Welch, D. Greenbaum, S. Mostame, and A. Aspuru-Guzik, *New J. Phys.* **16**, 033040 (2014).
- [57] Cirq Developers, Cirq (v0.14.1) (2022), doi: [10.5281/zenodo.6599601](https://doi.org/10.5281/zenodo.6599601).
- [58] A-tA-v *et al.*, Qiskit: An open-source framework for quantum computing (2021), doi: [10.5281/zenodo.2573505](https://doi.org/10.5281/zenodo.2573505).
- [59] N. Hansen and A. Ostermeier, *Evol. Comput.* **9**, 159 (2001).

- [60] M. Born and V. Fock, *Z. Phys.* **51**, 165 (1928).
- [61] T. Albash and D. A. Lidar, *Rev. Mod. Phys.* **90**, 015002 (2018).
- [62] M. H. S. Amin, *Phys. Rev. Lett.* **102**, 220401 (2009).
- [63] D. M. Tong, K. Singh, L. C. Kwek, and C. H. Oh, *Phys. Rev. Lett.* **98**, 150402 (2007).
- [64] S. Boixo and R. D. Somma, *Phys. Rev. A* **81**, 032308 (2010).
- [65] H. Cao, Z. Guo, Z. Chen, and W. Wang, *Sci. China Phys. Mech. Astron.* **56**, 1401 (2013).
- [66] H. Buhrman, R. Cleve, J. Watrous, and R. de Wolf, *Phys. Rev. Lett.* **87**, 167902 (2001).
- [67] I. Shavitt and L. T. Redmon, *J. Chem. Phys.* **73**, 5711 (1980).